



Fast-diffusing p75^{NTR} monomers support apoptosis and growth cone collapse by neurotrophin ligands

Laura Marchetti^{a,b,c,d,1,2}, Fulvio Bonfiglioli^{a,1}, Francesco Gobbo^{b,e,1}, Rosy Amodeo^{a,c}, Mariantonietta Calvello^b, Ajesh Jacob^b, Giovanni Signore^{a,c,3}, Chiara Schirripa Spagnolo^a, David Porciani^{a,c,4}, Marco Mainardi^b, Fabio Beltram^{a,3}, Stefano Luin^{a,f,2,5}, and Antonino Cattaneo^{b,2,5}

^aNational Enterprise for NanoScience and NanoTechnology (NEST) Laboratory, Scuola Normale Superiore, 56127 Pisa, Italy; ^bBio@SNS, Scuola Normale Superiore, 56124 Pisa, Italy; ^cCenter for Nanotechnology Innovation @NEST, Istituto Italiano di Tecnologia, 56127 Pisa, Italy; ^dDipartimento di Farmacia, Università di Pisa, 56126 Pisa, Italy; ^eCentre for Discovery Brain Sciences, University of Edinburgh, Edinburgh EH8 9JZ, United Kingdom; and ^fNEST, Istituto di Nanoscienze, Consiglio Nazionale delle Ricerche, 56127 Pisa, Italy

Edited by K. Christopher Garcia, Stanford University, Stanford, CA, and approved August 14, 2019 (received for review February 17, 2019)

The p75 neurotrophin (NT) receptor (p75^{NTR}) plays a crucial role in balancing survival-versus-death decisions in the nervous system. Yet, despite 2 decades of structural and biochemical studies, a comprehensive, accepted model for p75^{NTR} activation by NT ligands is still missing. Here, we present a single-molecule study of membrane p75^{NTR} in living cells, demonstrating that the vast majority of receptors are monomers before and after NT activation. Interestingly, the stoichiometry and diffusion properties of the wild-type (wt) p75^{NTR} are almost identical to those of a receptor mutant lacking residues previously believed to induce oligomerization. The wt p75^{NTR} and mutated (mut) p75^{NTR} differ in their partitioning in cholesterol-rich membrane regions upon nerve growth factor (NGF) stimulation: We argue that this is the origin of the ability of wt p75^{NTR}, but not of mut p75^{NTR}, to mediate immature NT (proNT)-induced apoptosis. Both p75^{NTR} forms support proNT-induced growth cone retraction: We show that receptor surface accumulation is the driving force for cone collapse. Overall, our data unveil the multifaceted activity of the p75^{NTR} monomer and let us provide a coherent interpretative frame of existing conflicting data in the literature.

p75 neurotrophin receptor | membrane oligomeric state | single-molecule microscopy | apoptosis | growth cone collapse

The p75 neurotrophin (NT) receptor (p75^{NTR}) is a single-pass transmembrane (TM) receptor of the tumor necrosis factor (TNF) receptor superfamily (1). Along with the Trk tyrosine kinase receptor (2) and the Vps10p domain-sorting receptor families (3), p75^{NTR} binds and is activated by NTs, small secreted homodimeric growth factors. NTs regulate survival, differentiation, and specification in developing neurons and plasticity and maintenance in adult neurons (4). This paradigmatic signaling system finely orchestrates 2 opposite pathways—survival versus death—in the central and peripheral nervous systems, and its alterations have a causal role in neurodegeneration (5, 6). Notably, p75^{NTR} is the only NT receptor with significant binding affinity for all NTs, as well as for their respective immature forms (proNTs) (1), thus playing a central role in their balance. The p75^{NTR} has long been considered a pan-NT coreceptor of Trk receptors, cooperating in the formation of high-affinity binding sites for NTs (7). However, the predicted ternary complex between NTs, Trk (or sorting receptors), and p75^{NTR} has never been observed with structural biology techniques, and the available crystal structures of the nerve growth factor (NGF)-TrkA (8) [and NGF-SorC2 (9)], NT-p75^{NTR} binary complexes have opposite orientations: This casts doubts on how a ternary complex could assemble (10). Available NT-p75^{NTR} structures are conflicting per se, as the NGF-p75^{NTR} cocrystal has 2:1 stoichiometry (11), while the NT3-p75^{NTR} cocrystal has 2:2 stoichiometry (12), with no obvious rationale for their difference. In addition, p75^{NTR} binds a number of ligands unrelated to NTs and has independent functions from Trks in controlling neurite outgrowth and morphology (13, 14), cell cycle withdrawal of developing neural

progenitors (15), and viral-related neuropathies (16). It is thus clear that the structural basis of p75^{NTR} signaling still needs proper understanding. On the basis of Western blot analysis from cell lysates, it was proposed that p75^{NTR} acts as a preformed disulfide-linked dimer via a conserved TM cysteine residue (Cys256 in human numbering, employed throughout this paper, corresponding to residues 257 in rat and 259 in mouse numberings), which would act as a fulcrum to propagate a conformational change from the p75^{NTR} extra- to intracellular domain upon NT binding (17). Cys256 mutation abolished NT-dependent apoptotic activity in cultured neurons and in a knock-in mouse model (18); however, this model was recently challenged by the report that this propagation of conformational changes could not be supported by the flexible p75^{NTR} juxtamembrane (JM) intracellular region (19). Furthermore, a similar Western blot analysis performed by Anastasia et al. (20) showed the existence of p75^{NTR} trimers, which are more represented than

Significance

Neurotrophins (NTs) are homodimeric growth factors displaying fundamental roles in the nervous system. Their activity stems from binding and activation of 3 different receptor types in nervous cell membranes. The p75 NT receptor (p75^{NTR}) was the first to be discovered in 1986; nevertheless, for the numerous structural and functional facets so far reported, its activation mechanisms have remained elusive. Here, we demonstrate that its pleiotropic functions are regulated by different redistributions of the receptors, which crucially depend on the available NT and on the involved subcellular compartment but are unrelated to its oligomerization state. Single-particle studies proved receptors to be monomers with a fast-diffusive behavior in the membrane with, at most, transient self-interactions on the millisecond time scale.

Author contributions: L.M., F. Bonfiglioli, F.G., F. Beltram, S.L., and A.C. designed research; L.M., F. Bonfiglioli, F.G., R.A., A.J., D.P., and M.M. performed research; M.C., G.S., and C.S.S. contributed new reagents/analytic tools; L.M., F. Bonfiglioli, F.G., R.A., F. Beltram, S.L., and A.C. analyzed data; and L.M., F. Bonfiglioli, F.G., F. Beltram, S.L., and A.C. wrote the paper.

The authors declare no conflict of interest.

This article is a PNAS Direct Submission.

This open access article is distributed under [Creative Commons Attribution-NonCommercial-NoDerivatives License 4.0 \(CC BY-NC-ND\)](https://creativecommons.org/licenses/by-nc-nd/4.0/).

¹L.M., F. Bonfiglioli, and F.G. contributed equally to this work.

²To whom correspondence may be addressed. Email: laura.marchetti@unipi.it, s.luin@sns.it, or antonino.cattaneo@sns.it.

³Present address: Fondazione Pisana per la Scienza, 56017 S. Giuliano Terme, Pisa, Italy.

⁴Present address: Department of Molecular Microbiology & Immunology, University of Missouri, Columbia, MO 65212.

⁵S.L. and A.C. contributed equally to this work.

This article contains supporting information online at www.pnas.org/lookup/suppl/doi:10.1073/pnas.1902790116/-DCSupplemental.

dimers; oligomerization, however, was not necessary for proNGF-induced growth cone collapse in developing neurons (20).

Here, we directly and quantitatively assess p75^{NTR} oligomerization status in the plasma membrane of living cells by means of single-molecule fluorescence microscopy with a minimally invasive strategy (21, 22); this relies on insertion of a short peptide tag in the p75^{NTR} protein and its labeling with 1:1 stoichiometry (23, 24). This method also allows imaging the receptor with small organic dyes, which, unlike the more cumbersome Quantum dots (Qdot), permits one to retrieve the receptor oligomeric state from their fluorescent intensity (21). We show that membrane p75^{NTR} is mostly a fast-diffusing monomer, regardless of NT stimulation. Its self-interactions are far too transient to result in substantial receptor di- or trimerization; importantly, they do not depend on Cys256 or on other residues previously suggested to play a role in receptor oligomerization. We also gather evidence on why the p75^{NTR} C256A mutant does not elicit NT-dependent apoptosis (18) but is functional for growth cone collapse signaling (20). By solving this apparent contradiction, we revisit here p75^{NTR} function, in the conceptual framework of a versatile monomeric receptor.

Results

Expression, Validation, and Membrane Fluorolabeling of Human p75^{NTR} Constructs. We previously demonstrated that p75^{NTR} can be enzymatically labeled with small chemical probes (e.g., biotin, organic fluorophores) in a site-specific way, inserting 12 amino acid-long tags of the ACP/PCP family at its N terminus (23). This allows a covalent modification with 1:1 stoichiometry (i.e., 1 probe per p75^{NTR} molecule) of the receptors exposed on the surface of living cells (24, 25). Here, we used S6-p75^{NTR} (Fig. 1A) for its better labeling performance when compared with A1-p75^{NTR} (SI Appendix, Fig. S1). We found that S6-p75^{NTR} correctly localizes on the plasma membrane, as well as on intracellular structures like the nuclear envelope, similar to endogenous p75^{NTR} expressed by PC12 cells (26) (Fig. 1B). Like endogenous p75^{NTR} (SI Appendix, Fig. S2), S6-p75^{NTR} undergoes palmitoylation (Fig. 1C), an important posttranslational modification for p75^{NTR} death domain signaling capability (27). The p75^{NTR} was recently reported to localize asymmetrically in neurons, helping in specifying the future axon (28); accordingly, biotinylated S6-p75^{NTR} receptors preferentially localize in neurites and growth cones in developing hippocampal neurons (Fig. 1D). Furthermore, S6-p75^{NTR}-EGFP was able to induce growth cone collapse in the same neurons upon proNGF administration (Fig. 1E), as reported for previous p75^{NTR} constructs devoid of chemical tags (29). Finally, proBDNF binding to p75^{NTR} was recently reported to increase the number of apoptotic neurons (18) (Fig. 1F, Top). By transducing S6-p75^{NTR} in cortical neurons from p75^{NTR} knockout (KO) mice (30) with an inducible lentiviral vector (24), we found that it was able to recapitulate proBDNF-induced apoptosis (Fig. 1F, Middle and Bottom). The lower percentage of apoptotic neurons, with respect to that raised by endogenous p75^{NTR}, is likely due to the presence of untransduced neurons.

Overall, our data demonstrate that the S6-tagged construct of human p75^{NTR} retains the properties of endogenous p75^{NTR}. We therefore employed it to visualize the p75^{NTR} membrane pool in living cells and to describe its behavior in a direct, unperturbed physiological way.

p75^{NTR} Single Molecules Diffuse as Monomers in the Cell Membrane. We first sought to investigate the membrane p75^{NTR} diffusive properties and oligomerization state in living cells. To this end, we expressed S6-p75^{NTR} in neuroblastoma SK-N-BE(2) cells, a line that conceivably models a neuronal membrane with the advantage of lacking endogenous p75^{NTR} and TrkA at both messenger RNA and protein levels (31). Once labeled with

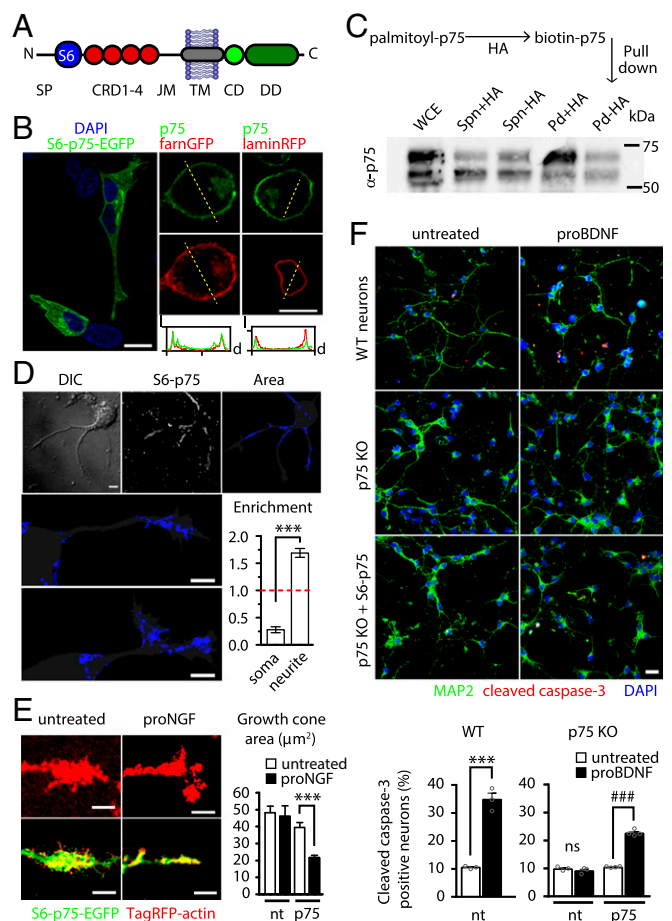


Fig. 1. Expression, validation, and membrane fluorolabeling of human p75^{NTR} constructs. (A) Scheme of the S6-p75^{NTR} construct. The S6 tag is inserted between the signal peptide (SP) and cysteine-rich domains 1 to 4 (CRD1-4). CD, chopper; DD, death domain. (B) S6-p75^{NTR}-EGFP (green) localizes in the plasma membrane and, to a minor extent, on the nuclear membrane in SHSY5Y cells (Left) as endogenous p75^{NTR} (green, Top Right) in PC12 cells expressing farnesyl (farn)-GFP or lamin-RFP (both red, Right). (Bottom Right) Intensity (I) vs. distance (d) plot along yellow dashed lines. (Scale bar, 10 μm.) (C) S6-p75^{NTR} is palmitoylated. (Top) Scheme of the hydroxylamine (HA)-catalyzed palmitoyl/biotin exchange. (Bottom) Western blot showing the streptavidin pulldown (Pd) and the corresponding nonpalmitoylated/biotinylated supernatant (Spn); the control reaction without HA is also shown. WCE, whole cell extract. (D) S6-p75^{NTR} is polarized in developing hippocampal neurons. The maximum intensity projection of a TIRF movie of Qdot-labeled S6-p75^{NTR} (white) and the area explored by S6-p75^{NTR} (blue) superimposed on the cell mask (gray) are shown. DIC, differential interference contrast. (Scale bars, 5 μm.) The graph shows the relative enrichment in the explored area in somas and neurites. ****P* < 0.001, paired Student's *t* test (2-tailed). Bars are mean ± SEM. The dotted red line is the value expected for a nonpolarized localization. (E, Left) Confocal images of growth cones of hippocampal neurons transfected with TagRFP-actin only (red, Top) or with S6-p75^{NTR} (green) and TagRFP-actin (Bottom), untreated or after 30 min of incubation with 20 ng/mL proNGF. (Scale bars, 5 μm.) (E, Right) Quantification of the growth cone area is reported in the graph. Bars are mean ± SEM. ****P* < 0.001, 1-way ANOVA (Bonferroni multiple comparisons). nt, nontransfected. (F, Top) Cleaved-caspase-3 (red)/MAP2 (green) immunofluorescence images to quantify proBDNF-induced apoptosis in cortical neurons from wt and p75 KO mice (DAPI is shown in blue). (Scale bar, 20 μm.) (F, Bottom) Percentage of cleaved caspase-3-positive neurons is reported as mean ± SEM in the graph. ****P* < 0.001, unpaired Student's *t* test (2-tailed); ###*P* < 0.001, 1-way ANOVA (Tukey's multiple comparisons). ns, not significant at the 0.05 level. nt, nontransduced.

Abberior635P dye (SI Appendix, Fig. S3), S6-p75^{NTR} imaged with total internal reflection fluorescence (TIRF) microscopy appears as a carpet of spots decorating the cell basal membrane,

each corresponding to a single receptor particle (Fig. 2*A* and *B*). With a Tet-On inducible promoter (24), we tuned receptor expression from low (~ 0.1 spot per square micrometer) to the highest density allowing us to track $p75^{\text{NTR}}$ receptors individually (~ 0.5 spot per square micrometer), and even to bulk $p75^{\text{NTR}}$ expression (Fig. 2*A*). Receptors at densities from 0.1 to 0.45 spot per square micrometer were followed over time (Movies *S1* and

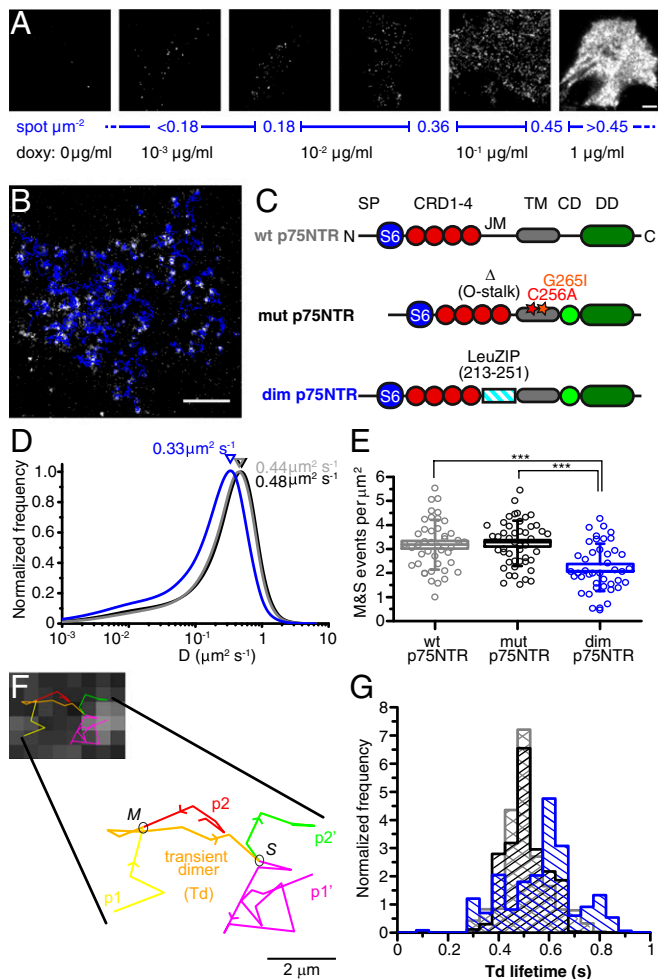


Fig. 2. Membrane dynamics of $p75^{\text{NTR}}$ molecules in the cell membrane. (*A*) Expression of S6- $p75^{\text{NTR}}$ regulated by doxycycline (doxy). TIRF images of Abberior635P-labeled $p75^{\text{NTR}}$ receptors in SK-N-BE(2) cells show the dependence of the number of receptors per area (blue scale) on doxycycline concentration in the medium (black values below). (Scale bar, 5 μm .) (*B*) TIRF image of S6- $p75^{\text{NTR}}$ labeled with Abberior635P; superimposed trajectories are shown in blue. (Scale bar, 5 μm .) (*C*) S6-tagged constructs. The wt $p75^{\text{NTR}}$ is as in Fig. 1*A*; mut $p75^{\text{NTR}}$ bears mutations C256A and G265I, and lacks residues 221 to 246 encompassing the O-stalk domain in the JM region; and dim $p75^{\text{NTR}}$ has residues 213 to 251 of the JM portion replaced with the leucine zipper domain (LeuZIP) from c-jun. CD, chopper; DD, death domain; SP, signal peptide. (*D*) Distribution of D for wt $p75^{\text{NTR}}$ (gray), mut $p75^{\text{NTR}}$ (black), and dim $p75^{\text{NTR}}$ (blue). (*E*) Number of M&S events in 500-frame movies, normalized per membrane area, for wt $p75^{\text{NTR}}$ (gray), mut $p75^{\text{NTR}}$ (black), and dim $p75^{\text{NTR}}$ (blue). Boxes represent SE, lines represent median, and whiskers represent SD. $***P < 0.001$, Kruskal–Wallis test. (*F*) TIRF frame with superimposed transient dimer trajectory, enlarged at the bottom for visualizing the merge (*M*) between $p1$ (yellow) and $p2$ (red) particles, their colocalization trajectory (orange) corresponding to a transient dimer (*Td*), and their split (*S*) in $p1'$ (magenta) and $p2'$ (green) particles. (Scale bar, 2 μm .) (*G*) Distribution of the cell-average duration of *Td* trajectories for wt $p75^{\text{NTR}}$ (gray), mut $p75^{\text{NTR}}$ (black), and dim $p75^{\text{NTR}}$ (blue) constructs. Cells with 0.18 to 0.36 receptor per square micrometer range were considered for these analyses.

S2), and tracked at the single-particle level (32) (Fig. 2*B* and Movie *S3*). We compared wild-type $p75^{\text{NTR}}$ (wt $p75^{\text{NTR}}$; Fig. 2*C*) with 2 reference monomeric or dimeric variants of S6-tagged $p75^{\text{NTR}}$. The “monomeric” form contains C256A and G265I mutations on the $p75^{\text{NTR}}$ TM domain, which were reported to inhibit covalent and noncovalent receptor dimerization, respectively (17), along with a deletion in its JM region that inhibits intracellular clustering (33) (mutant $p75^{\text{NTR}}$ [mut $p75^{\text{NTR}}$]; Fig. 2*C*). The mut $p75^{\text{NTR}}$ recapitulated the localization observed for wt $p75^{\text{NTR}}$ (*SI Appendix*, Fig. *S4A* and *B*); importantly, it did not display the high-molecular-weight bands in Western blots (*SI Appendix*, Fig. *S4C*) previously identified as putative receptor oligomeric forms (17, 20). To force dimerization, we replaced the entire wt $p75^{\text{NTR}}$ extracellular JM region with the c-jun leucine-zipper domain, as in a study by Brooks et al. (34) (dim $p75^{\text{NTR}}$; Fig. 2*C*).

In SK-N-BE(2) cells, analysis of the short-time diffusion coefficient (D) distributions, as in studies by Marchetti et al. (21) and Callegari et al. (25), revealed that wt $p75^{\text{NTR}}$ and mut $p75^{\text{NTR}}$ are indistinguishable, while dim $p75^{\text{NTR}}$ is significantly slower, showing a distribution shifted toward D values compatible with what is expected for dimers (35) and a somewhat higher low- D tail (Fig. 2*D*); these data suggest the absence of stable dimers for both wt $p75^{\text{NTR}}$ and mut $p75^{\text{NTR}}$. To identify possible transient $p75^{\text{NTR}}$ dimers, we analyzed the dynamic association/dissociation of spots during their trajectories (merge and split [M&S] events, shown in Movies *S4* and *S5* and schematized in Fig. 2*F*), as previously done by Kasai and Kusumi (36). The number of M&S events per membrane area was significantly lower for dim $p75^{\text{NTR}}$ than for wt $p75^{\text{NTR}}$ and mut $p75^{\text{NTR}}$; the latter 2, instead, did not differ significantly (Fig. 2*E*). This shows that the 3 $p75^{\text{NTR}}$ constructs display an observable dynamic equilibrium between monomers and dimers, but while wt $p75^{\text{NTR}}$ has association/dissociation kinetics similar to mut $p75^{\text{NTR}}$, dim $p75^{\text{NTR}}$ has either a higher dimerization probability or a lower separation rate. We also quantified the mean duration of transient dimerization (T_d) events (orange in Fig. 2*F*), i.e., the trajectory segments between a merge event and a split event. The distribution of average T_d lifetime demonstrated that while wt $p75^{\text{NTR}}$ and mut $p75^{\text{NTR}}$ display dimerization events equally peaked between 0.4 and 0.5 s, those of dim $p75^{\text{NTR}}$ peak at 0.6 and 0.8 s (Fig. 2*G*). These results allow us to determine that wt $p75^{\text{NTR}}$ does not form stable dimers or higher oligomers in the living cell membrane.

Because of the transient nature of $p75^{\text{NTR}}$ dimers, as well as of photobleaching during tracking, analysis of the average intensity of the trajectories in live cells could not give an unambiguous answer on the stoichiometry (*SI Appendix*, Fig. *S5*). Therefore, we analyzed the intensity step photobleaching profile of isolated $p75^{\text{NTR}}$ /Abberior635P spots in fixed cells (yellow boxes in Fig. 3*A*). For each spot, we quantified 1) the number of photobleaching steps (red arrows in Fig. 3*B*) and 2) the mean intensity before bleaching (I_{PRE} ; green lines in Fig. 3*B*). Both constitute a direct measure of the number of molecules in a spot for receptor membrane oligomerization (37). The vast majority of analyzed wt $p75^{\text{NTR}}$ and mut $p75^{\text{NTR}}$ spots are monomers; that is, they display 1 photobleaching step (about 77% for both species; Fig. 3*C*). Conversely, the NGF-stimulated S6-TrkA construct displayed a significantly higher proportion of dimers and oligomers (26) (*SI Appendix*, Fig. *S6A*). Importantly, the majority of dim $p75^{\text{NTR}}$ spots showed a 2-step photobleaching profile (55%; Fig. 3*C*), and monomers were reduced to 35%. Only dim $p75^{\text{NTR}}$ displayed a sizeable amount of spots with 3 and 4 photobleaching steps. I_{PRE} distributions obtained for the 3 $p75^{\text{NTR}}$ variants confirmed the bleaching step analysis (*SI Appendix*, Fig. *S6B*).

We underline that some mut $p75^{\text{NTR}}$ apparent dimers were detected (about 20% of the analyzed spots) similar to wt $p75^{\text{NTR}}$. This proves the lack of a relationship with the TM residues previously indicated as driving receptor dimerization (17). Overall,

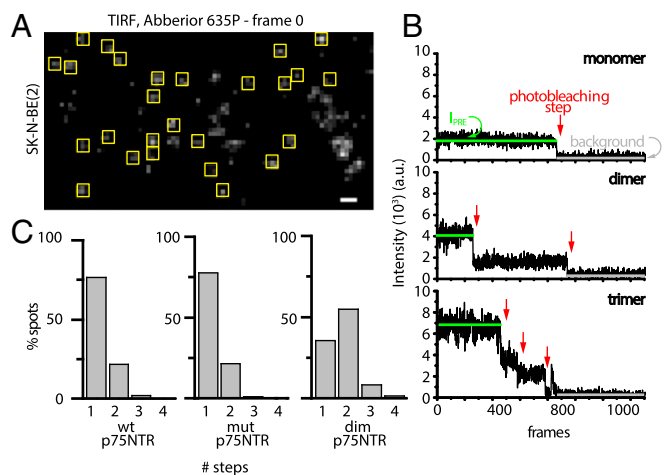


Fig. 3. p75^{NTR} is predominantly a monomer in the cell membrane. (A) TIRF image showing receptor spots on the surface of fixed cells (yellow squares represent analyzed spots; analyzed cells had 0.2 to 0.5 spot per square micrometer). (Scale bar, 1 μm .) (B) Typical intensity profile traces of a monomer (Top), dimer (Middle), and trimer (Bottom) showing the parameters considered in the calculation. I_{PRE} (green line) is the particle average intensity before the first bleaching step, red arrows point to single photobleaching steps, and the gray line represents background intensity. a.u., arbitrary units. (C) Photobleaching steps per trace for wt p75^{NTR}, mut p75^{NTR}, and dim p75^{NTR}.

our experiments distinguish between the diffusivity of monomers and dimers, and challenge the existence of stable p75^{NTR} dimers in the membrane of live cells.

wt p75^{NTR} and mut p75^{NTR} Display Different Membrane Partitioning in Response to NGF Stimulation. We next compared wt p75^{NTR} and mut p75^{NTR} membrane diffusivity following NT stimulation, to see if this might impact the oligomeric state of the receptor. Also, we aimed at identifying a possible molecular basis, an alternative to the lack of oligomerization, as the source of the impaired apoptotic signaling of mut p75^{NTR} following NT stimulation (17, 18).

We measured D values from trajectories of wt p75^{NTR} and mut p75^{NTR} with or without 15 min of NGF stimulation. The diffusivity of both constructs upon NGF treatment remained significantly higher than that of the dim p75^{NTR} construct (Fig. 4A). This suggests that NGF does not induce dimerization of either construct. These data are consistent with the absence of fluorescence resonance energy transfer (FRET) or homo-FRET changes following NT addition in cells expressing fluorescent p75^{NTR} constructs (17, 38). However, NGF elicits a small but statistically significant shift of D distributions of the 2 constructs in opposite directions (i.e., it slightly slows down wt p75^{NTR}, while it speeds up mut p75^{NTR}). Similarly, a slowing down of wt p75^{NTR} was observed in proNGF-treated neurons (SI Appendix, Fig. S7). Since these changes are not compatible with gain or loss of stable oligomerization, we reasoned that they might stem from wt p75^{NTR} and mut p75^{NTR} movements across membrane areas with different composition. In this scenario, lipid rafts may represent the discriminating factor, as they could confine and alter transiently the diffusivity of membrane proteins (39). Cholesterol plays a key structural role in lipid rafts, and the association of proteins with lipid rafts can be detected experimentally by testing cholesterol-dependent, confined diffusion (40). Consistently with this, p75^{NTR} mobility was found to depend on the cholesterol content in the plasma membrane (41), and we measured a clear anticorrelation between its D value and membrane cholesterol in 6 cellular models (Fig. 4B and SI Appendix, Fig. S8). The fastest p75^{NTR} diffusivity is observed in cortical neurons, which display the lowest membrane cholesterol

levels of our survey; SK-N-BE(2) cells have a cholesterol content similar to neurons, thus validating the choice of this model system to study p75^{NTR} membrane dynamics.

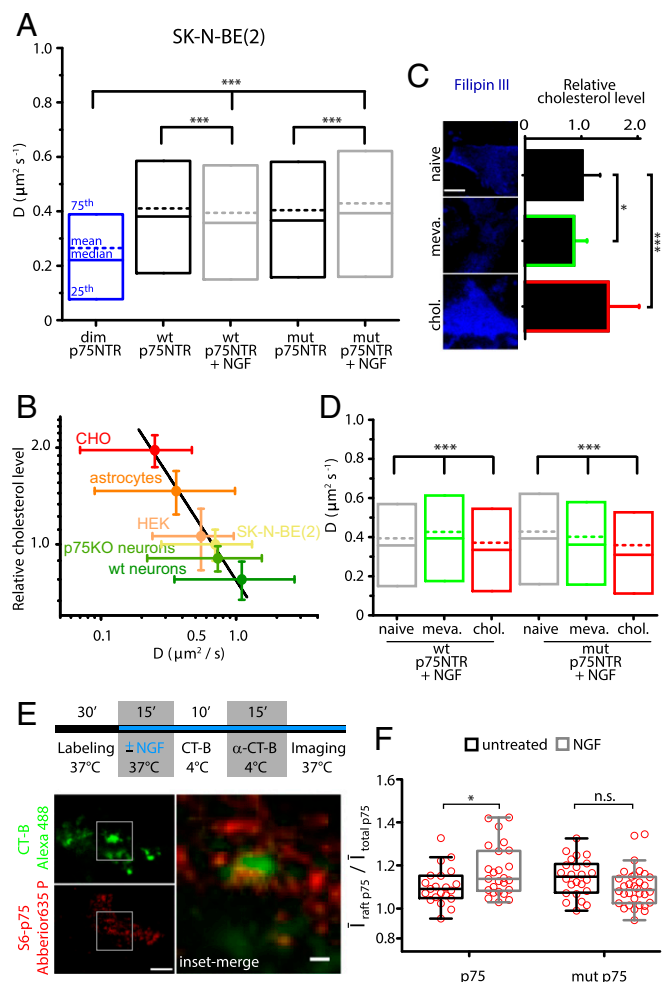


Fig. 4. Membrane cholesterol regulates p75^{NTR} diffusivity and response to NGF. (A) Box-plot for D values from trajectories of wt p75^{NTR} or mut p75^{NTR} in SK-N-BE(2) cells in resting conditions (black) and up to 15 min after NGF administration (gray); the distribution for dim p75^{NTR} (blue) is also shown. Boxes represent 25th to 75th percentiles, lines represent medians, and dashed lines represent means. *** $P < 0.001$, Kruskal-Wallis test (with Dunn's means comparison). (B) Plot of membrane cholesterol (CHO) content (mean intensity \pm SEM of filipin III-stained cells) versus D of p75^{NTR} single molecules (peak \pm full width at half maximum of its distribution as in SI Appendix, Fig. S8C) in 6 different cell models. Cholesterol content is normalized to SK-N-BE(2) cell results. The black line indicates linear fit. HEK, human embryonic kidney 293 cells. (C) TIRF images of filipin III-stained SK-N-BE(2) cells exhibiting modulation of cholesterol levels (quantified as mean intensity \pm SEM) with mevastatin (meva., green) or soluble cholesterol (chol., red). * $P < 0.05$ and *** $P < 0.001$, 1-way ANOVA. (D) Same graph as in A, obtained for NGF-stimulated wt and mut p75^{NTR} cells in SK-N-BE(2) cells (gray), treated with mevastatin (green) and cholesterol (red). *** $P < 0.001$, Kruskal-Wallis test (with Dunn's means comparison). (E) Outline of the colocalization experiment with TIRF images of cholera toxin B subunit (CT-B)-stained GM1 (green) and p75^{NTR} single molecules (red). (Scale bar, 5 μm ; Inset, 1 μm .) (F) Quantification of wt/mut p75^{NTR} and CT-B colocalization in the absence or presence of NGF. Box-plots show median and 25th to 75th percentiles of average p75^{NTR} intensity inside CT-B-stained domains ($I_{\text{raft p75}}$) over average p75^{NTR} intensity within the whole cell ($I_{\text{total p75}}$). Whiskers indicate Tukey intervals, and red circles represent individual data. * $P = 0.016$, 1-way ANOVA (with Bonferroni comparison of means). ns, not significant at the 0.05 level.

Given that raft domains are crucial for apoptotic signaling via p75^{NTR} (42), we considered that differential residency of wt p75^{NTR} and mut p75^{NTR} upon NT binding in these areas might explain not only the D changes observed (Fig. 4A) but also their different signaling abilities. To test this hypothesis, we first monitored NGF-driven diffusivity of the 2 receptor forms following up- or down-regulation of membrane cholesterol in SK-N-BE(2) cells (Fig. 4C). While increasing membrane cholesterol slows down both receptor forms, removal of membrane cholesterol has 2 opposite outcomes: wt p75^{NTR} is accelerated, while mut p75^{NTR} slowed (Fig. 4D). Since the effect of cholesterol depletion on lateral diffusion depends on the composition of the membrane regions explored by the membrane receptors (43), these data suggest that wt p75^{NTR} and mut p75^{NTR} partition into different membrane areas after NGF binding. These relocalizations most probably occur in a very dynamic way, given the small diffusivity changes involved (Fig. 4A and *SI Appendix, Fig. S7*). Indeed, biochemical isolation of raft domains showed wt p75^{NTR} localizing in both raft and nonraft regions, in the absence and presence of NGF (44, 45). Thus, to capture transient raft occupancy, we imaged lipid rafts and p75^{NTR} simultaneously, after 15 min of NGF stimulation, by dual-color TIRF microscopy (Fig. 4E), similar to the method used by Pinaud et al (46). Rafts were visualized by cross-linking membrane ganglioside GM1 with a fluorescent cholera toxin B subunit (47). NGF stimulation significantly increases the localization of wt p75^{NTR} in GM1 regions, but not that of mut p75^{NTR} (Fig. 4F).

We conclude that p75^{NTR} translocates to lipid rafts upon NGF binding, and mut p75^{NTR} has a reduced residency in cholesterol-rich membrane microdomains upon NGF binding compared with the wt counterpart. Notably, in the absence of competing Trk receptors, both NTs and proNTs induce coherent effects on p75^{NTR} in terms of both membrane diffusivity (Fig. 4A and *SI Appendix, Fig. S7*) and biological activity; for instance, proBDNF induces apoptosis via p75^{NTR} (18), but p75^{NTR} also mediates apoptosis in retinal neurons by NGF (48) and in sympathetic neurons by BDNF (49).

Membrane Cholesterol Regulates p75^{NTR} Apoptotic Signaling. Following previous observations, we tested if membrane cholesterol levels also affected NT-dependent apoptotic signaling via p75^{NTR}; here, C256 TM residue was shown to play a crucial role (17, 18). Treating neurons with mevastatin and methyl-beta-cyclodextrin (M β CD) strongly decreases membrane cholesterol, as measured by filipin staining, while loading neurons with cholesterol has the opposite effect (Fig. 5A and B). The proBDNF-induced apoptosis was abolished in cholesterol-depleted cortical neurons from wt mice, while it was slightly increased upon cholesterol overload (Fig. 5C). Cholesterol modulation was also applied to wt p75^{NTR} and mut p75^{NTR} (Fig. 5D–F) transduced in p75^{NTR} KO mouse neurons and induced with 0.05 μ g/mL doxycycline, a concentration not leading to overexpression (Fig. 2A). The p75^{NTR} KO neurons were not responsive to proBDNF; wt p75^{NTR}, but not mut p75^{NTR}, restored proapoptotic signaling (Fig. 5D). When neurons were treated with mevastatin/M β CD, wt p75^{NTR} lost its ability to induce apoptosis, confirming our results on wt neurons (Fig. 5C and E). Conversely, cholesterol administration boosted proapoptotic signaling of wt p75^{NTR} (Fig. 5F and G); surprisingly, the same treatment also conferred apoptotic capability to mut p75^{NTR} (Fig. 5F and G). This was not an effect of the combination of proBDNF and cholesterol load: Untransduced neurons from p75^{NTR} KO mice were not responsive in these conditions (Fig. 5F).

From these results, we conclude that the inability of mut p75^{NTR} to induce apoptosis (18) (Fig. 5D) is due to its poorer occupancy of cholesterol-rich membrane regions when compared with wt p75^{NTR}, rather than to impaired signaling of the protein per se. Accordingly, under membrane-saturating conditions obtained inducing p75^{NTR} expression with 1 μ g/mL doxycycline

(Fig. 2A), both mut p75^{NTR} and wt p75^{NTR} were able to induce apoptosis (*SI Appendix, Fig. S9*). These findings, along with those obtained in SK-N-BE(2) cells (Fig. 4), show that NT binding regulates the partitioning of p75^{NTR} in and out of lipid rafts, thereby regulating its ability to induce apoptosis.

Surface-Exposed p75^{NTR} Mediates Growth Cone Collapse in the Presence and Absence of proNGF. Growth cone retraction caused by overexpression of both wt p75^{NTR} and a C256A p75^{NTR} mutant was reported to occur upon proNGF administration in developing neurons (20). Hence, p75^{NTR} collapse action may not necessarily depend on receptor partitioning in cholesterol-rich regions, unlike apoptotic signaling (Fig. 5). We therefore investigated the mechanisms of axonal growth regulation by p75^{NTR}. We found that endogenous levels of p75^{NTR} can also regulate axon branching. Axonal arbors of CA3 neurons projecting into the CA1 region are significantly more ramified and occupy larger areas in p75^{NTR} KO mice than in wt mice (*SI Appendix, Fig. S10A and B*). This is reflected in a higher number of synaptic boutons (*SI Appendix, Fig. S10C*), consistent with previous observations of p75^{NTR} KO animals showing increased dendritic complexity (50). Neuronal cultures of the same animals recapitulated this result (Fig. 6A and B), with p75^{NTR} KO axons being longer (Fig. 6C) and displaying an increased number of branch points (Fig. 6D) and lateral growth cones per length unit (Fig. 6E) with respect to wt axons. Importantly, transient expression of wt p75^{NTR} or mut p75^{NTR} constructs in p75^{NTR} KO neurons completely rescued the phenotype observed in wt neurons (Fig. 6C–E). In agreement with previous data (20), expression of either wt p75^{NTR} or mut p75^{NTR} in hippocampal neurons leads to growth cone collapse in response to proNGF (*SI Appendix, Fig. S11A and B*). Overall, this suggests that the regulation of axonal complexity and proNT-dependent collapse of growth cones share a common mechanism regulated by p75^{NTR} independently on Cys256 and other residues mutated or missing in mut p75^{NTR} (Fig. 2C).

To gain further insight into this mechanism, we monitored the membrane pool of S6-p75^{NTR}-EGFP during collapse by biotinylation the receptors on the cell surface before proNGF incubation, and detecting receptors still present on the plasma membrane with streptavidin-Qdot after proNGF incubation for 30 min; EGFP fluorescence marked the total content of p75^{NTR} (Fig. 7A). The proNGF caused a dramatic increase in the membrane pool of both wt p75^{NTR} and mut p75^{NTR}, while lower levels of membrane p75^{NTR} were detected in untreated neurons (Fig. 7B and C). Inhibition of dynamin-dependent internalization with Dynasore (Fig. 7D), to maintain wt and mut S6-p75^{NTR}-EGFP on the surface regardless of proNGF administration (Fig. 7E), was sufficient to drive the growth cone collapse, independently from ligands; indeed, proNGF had no further collapse-inducing effect, implying that p75^{NTR} exposure is a downstream event to ligand binding (Fig. 7F and *SI Appendix, Fig. S11A*). Notably, Dynasore alone in untransfected neurons did not have such a prominent effect, although a trend could be observed upon drug treatment and proNGF administration (Fig. 7F); this is likely due to a fraction of hippocampal neurons expressing detectable levels of p75^{NTR}, as previously shown (29). Inhibiting p75^{NTR} internalization by expressing the K44A dominant negative form of dynamin had the same effect (*SI Appendix, Fig. S11D and E*), confirming the results obtained with Dynasore. Furthermore, we found that the mechanism responsible for the removal of p75^{NTR} from the plasma membrane in the absence of proNGF is dependent on clathrin, as blocking clathrin-dependent endocytosis by Pitstop2 was sufficient to accumulate surface p75^{NTR} and trigger neuronal growth cone collapse (Fig. 7G–J).

These data suggest that p75^{NTR} has an intrinsic collapsing activity when retained on the growth cone membrane, and internalization inhibition is a sufficient driving force that does not

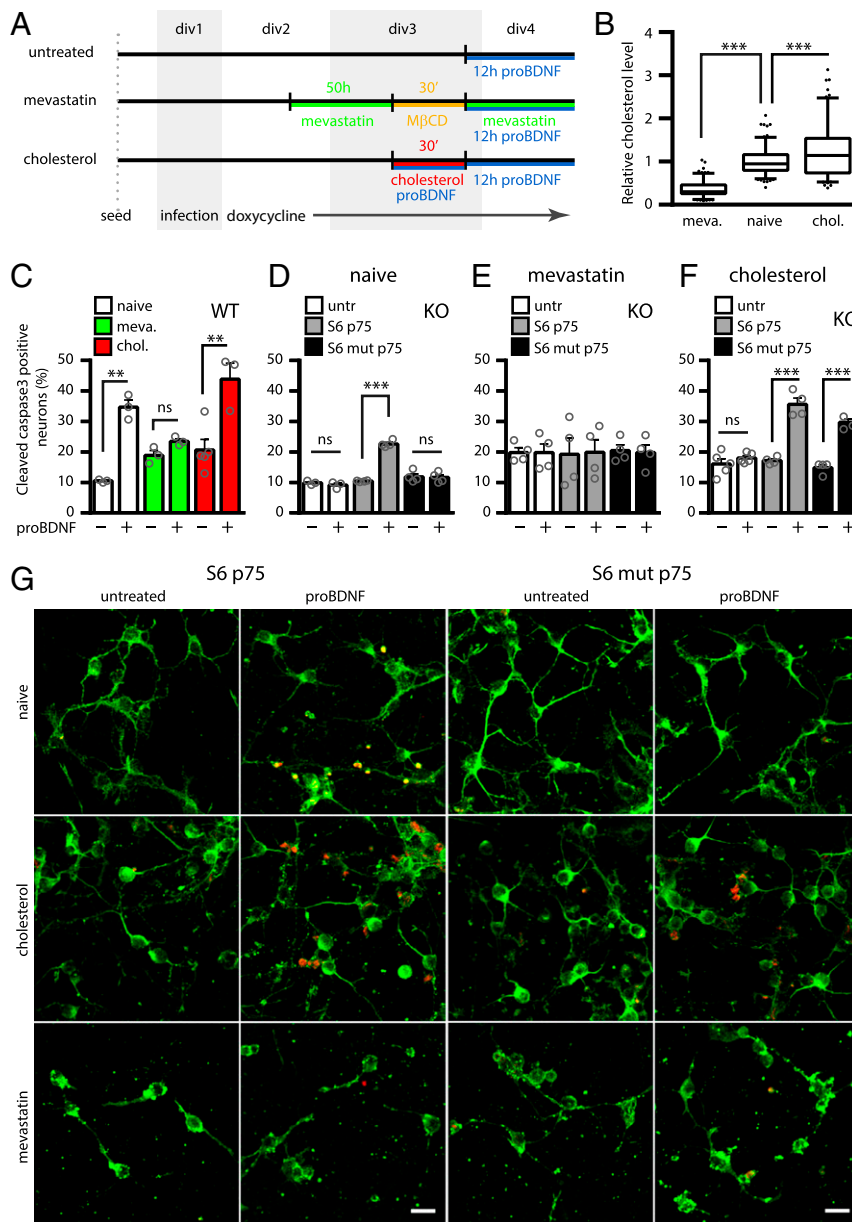


Fig. 5. Membrane cholesterol regulates proBDNF apoptotic signaling via p75^{NTR}. Experimental timeline (A) and quantification of cholesterol (intensity of filipin III staining) in cortical neurons treated with mevastatin/M β CD (meva.) or soluble cholesterol (chol.), relative to untreated neurons (B). ****P* < 0.001, 1-way ANOVA (Tukey's multiple comparisons). Box-plots represent 25th to 75th percentiles, whiskers indicate Tukey intervals, and dots represent outliers. div, day in vitro. (C) Percentage of cleaved caspase-3-positive neurons in wt cortical neurons (naive, white columns) or in the same neurons treated with mevastatin (green columns) or cholesterol load (red columns) in the absence or presence of proBDNF. (D) Percentage of cleaved caspase-3-positive neurons in untransduced p75^{NTR} KO cortical neurons (untr [untransduced], white columns) or in the same neurons transduced with wt p75^{NTR} (gray columns) or mut p75^{NTR} (black columns) and induced with 0.05 μ g/mL doxycycline, with or without proBDNF. White and gray columns are reported from Fig. 1F. The same is shown in conditions of cholesterol depletion (E, mevastatin) and cholesterol load (F, cholesterol) of the neurons. For C–F, ***P* < 0.01 and ****P* < 0.001, 1-way ANOVA test (with Tukey's comparison of means). ns, not significant at the 0.05 level. Bars are mean \pm SEM, and superimposed dots represent samples. (G) Representative confocal images of neurons expressing wt p75^{NTR} or mut p75^{NTR}, untreated or treated with proBDNF. Naive neurons (Top), cholesterol-enriched (cholesterol) neurons (Middle), and cholesterol-depleted (mevastatin) neurons (Bottom) are shown. MAP2 (green) and cleaved caspase-3 (red) are indicated. (Scale bars, 20 μ m).

necessarily require NT-induced partitioning into raft domains. Indeed, both wt p75^{NTR} and mut p75^{NTR} constructs similarly regulate axonal complexity. Overexpression has been called into question in the evaluation of growth cone collapse (18). Indeed, p75^{NTR} expression by a constitutively strong promoter results in a many-fold expression increase compared with that of p75^{NTR} induced at 0.05 μ g/mL doxycycline (SI Appendix, Fig. S12), which recapitulates the behavior of endogenous p75^{NTR} (Fig. 5). We therefore evaluated the effect of proNGF on neurons infected with

wt p75^{NTR} or mut p75^{NTR} and induced with 0.05 μ g/mL or 1 μ g/mL doxycycline (SI Appendix, Fig. S13A). We found that growth cone collapse could still be observed, although at lower levels than with overexpressed p75^{NTR}. The growth cone area decreases with increasing surface p75^{NTR} density: In particular, a threshold for growth cone collapse was found in the range of 1 to 2 receptors per square micrometer (SI Appendix, Fig. S13 B and C). Although slightly higher than the receptor ranges explored in our advanced imaging (Fig. 3 and SI Appendix, Fig. S7) and apoptosis assays (Fig.

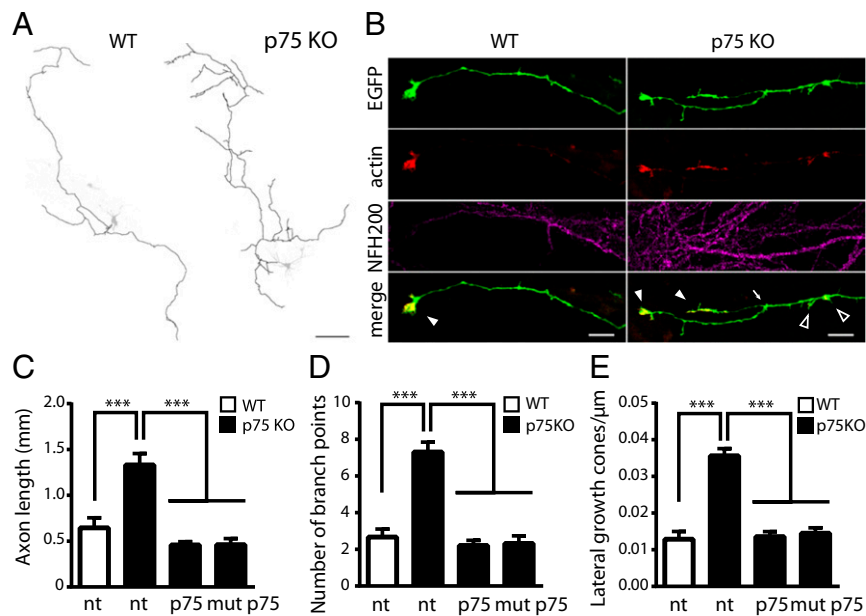


Fig. 6. wt p75^{NTR} and mut p75^{NTR} mediate growth cone collapse and regulate axon complexity. (A) Hippocampal neurons from wt (Left) and p75^{NTR} KO (Right) mice. Axons from EGFP- and TagRFP-actin-expressing neurons are drawn in black and superimposed to the EGFP channel (grayscale). (Scale bar, 100 μm.) (B) Magnification of axon terminals from images in A also showing immunofluorescence for the axonal marker NF-200. TagRFP-actin accumulates at growth cones. Branching points (arrow), terminal growth cones (filled arrowheads), and lateral growth cones (empty arrowheads) are indicated. (Scale bars, 5 μm.) Quantification of axon length (C), number of branch points (D), and number of lateral growth cones per length unit (E) are illustrated in non-transfected (nt) wt hippocampal neurons (white columns), in nt p75^{NTR} KO hippocampal neurons (black columns), or transfected with wt p75^{NTR} or mut p75^{NTR} constructs (wt/mut p75^{NTR}, black columns). ****P* < 0.001, Kruskal–Wallis test (Dunn’s multiple comparisons). Bars are mean ± SEM.

5), this value seems compatible with physiological levels observed at least in a subset of central neurons displaying sufficient p75^{NTR} levels to drive cone retraction (29). At 0.05 μg/mL doxycycline, p75^{NTR} explores a range of expression levels on the neuronal surface, with densities spanning from below to above the range of 1 to 2 receptors per square micrometer, and this explains why only a subpopulation of neurons undergoes growth cone collapse in this sample (*SI Appendix, Fig. S13*). Importantly, the growth cone area distribution for mut p75^{NTR} neurons was not significantly different from that for wt p75^{NTR}, and the 2 forms displayed similar area versus p75^{NTR} level dependency (*SI Appendix, Fig. S13C*), thus ruling out overexpression as the cause for their identical behavior (Fig. 6). This demonstrates that growth cone collapse via p75^{NTR} can occur at receptor levels close to or slightly higher than the natural average density in neurons, and that both p75^{NTR} forms are equally capable of mediating it.

Discussion

To solve the oligomerization conundrum of p75^{NTR} in a live cell context and to gain insight into its mechanisms of activation by NTs, we applied a single-molecule fluorescence approach that we had already validated to image and track NT receptors and their ligands (21–25). This avoids the use of indirect methods like labeled antibodies or ligands and obviates the problem of Qdot steric hindrance (51) (*SI Appendix, Fig. S3*). In neuroblastoma cells (*Movie S1* and Figs. 2D and 4A), as well as in primary neurons (Fig. 4B, *SI Appendix, Fig. S7*, and *Movie S2*), p75^{NTR} exhibits fast dynamics and is mostly present in monomeric form. NT or proNT stimulations do not alter its stoichiometry significantly (Figs. 3 and 4A); instead, our data show that p75^{NTR} molecules only form transient homointeractions if any (Figs. 2E–G and 3), indicating that dynamic interactions are likely to underlie receptor activation.

The existence of preformed p75^{NTR} oligomers in the membrane has been hotly debated, with different groups reporting

p75^{NTR} dimers (1, 17), trimers (13), or a mixture of both (16, 20). Evidence for oligomerization mostly came from the electrophoretic shift of the immunodetected receptor band of 2- or 3-fold the weight of the monomer, in nonreducing conditions or after chemical cross-linking. However, this constitutes an indirect way of investigating stoichiometry. Indeed, both run length and intensity of higher weight bands in a gel critically depend on several technical parameters, such as lysis conditions, antibody, or composition of the gel (*SI Appendix, Table S1* and compare, e.g., *SI Appendix, Figs. S4* and *S14*). Heavier p75^{NTR}-immunoreactive bands may be the result of p75^{NTR} homo- or hetero-aggregation with unknown proteins or lipids in close proximity. Indeed, p75^{NTR} association with gangliosides in response to ligands was already reported (52). Thus, the shifted bands could simply reflect crowding of molecules interacting transiently in cholesterol-rich regions, which are stabilized by certain lysis conditions, rather than a stable physical association. This is supported by the recent observation that the putative oligomeric shifted band of another TNF receptor, Death Receptor 5, is impaired by cholesterol-depletion treatments (53). Here, we provide a direct and quantitative estimate of the human full-length p75^{NTR} oligomerization state in the cell membrane. Our data on dynamics and bleaching steps demonstrate a predominant monomeric p75^{NTR} form (~77%; Fig. 3B). Notably, this percentage is almost identical (Fig. 3B), as is the diffusive profile (Fig. 2D–G), to a reference monomeric p75^{NTR} construct (mut p75^{NTR}), which bears all mutations impairing p75^{NTR} gel-shifted bands (17, 20, 33) (Fig. 2C). Therefore, even if ~22% of p75^{NTR} apparent dimers are detected, they are not dependent on the mutated or deleted residues; this fraction likely constitutes an overestimation due to nonresolved pairs of individual monomers merely in proximity, especially in small zones on the membrane where diffusivity is hindered; a similar effect could also explain the presence of trimers and tetramers for dim p75^{NTR}. For G protein-coupled receptors, apparent oligomers

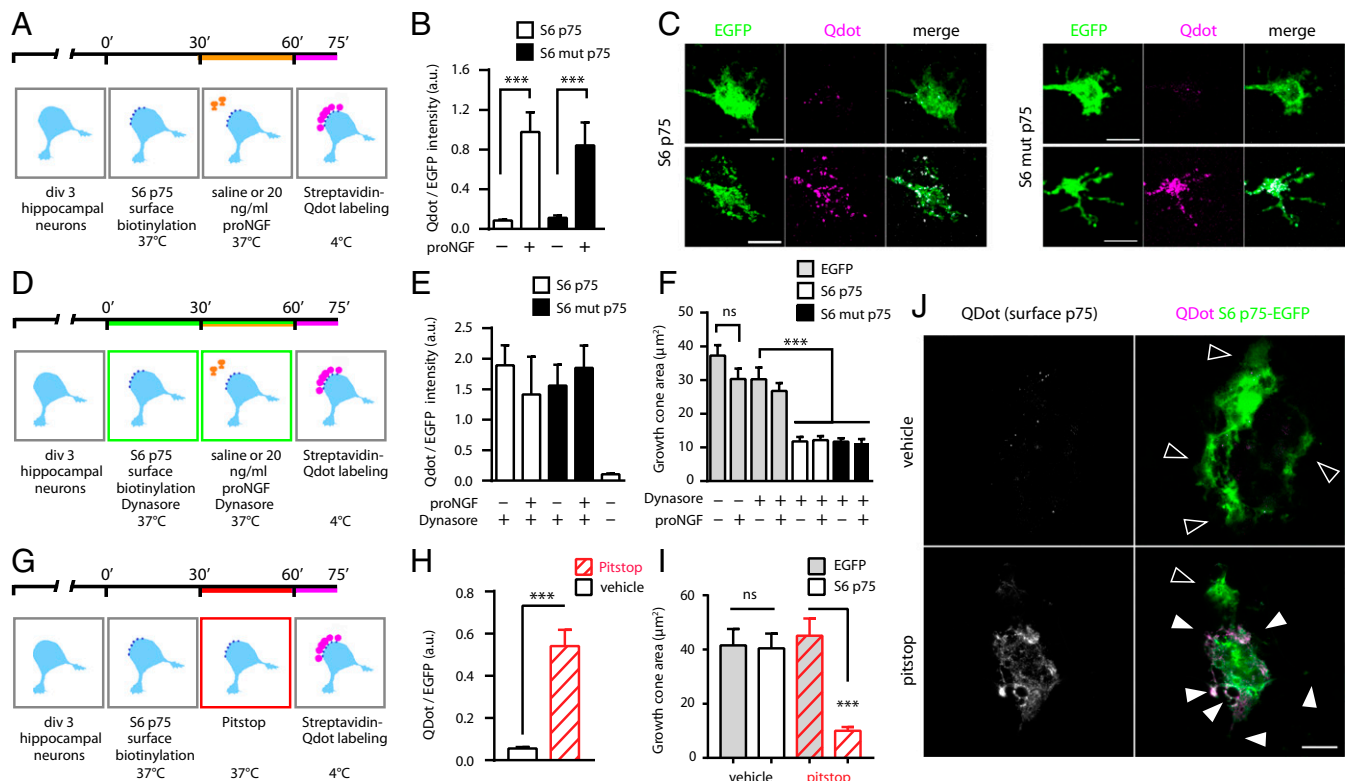


Fig. 7. Surface-exposed p75^{NTR} mediates growth cone collapse in the presence and absence of proNGF. (A) Timeline of the experiment to detect surface S6-p75^{NTR}-EGFP after proNGF administration. (B) Qdot-to-EGFP ratio is a measure of surface p75^{NTR}-EGFP. Both wt p75^{NTR} and mut p75^{NTR} are enriched on the plasma membrane after 30 min of proNGF treatment. ****P* < 0.001, Kruskal–Wallis test (Dunn’s multiple comparisons). Bars are mean ± SEM. a.u., arbitrary units. (C) Confocal images of growth cones of wt hippocampal neurons, transfected with S6-tagged wt p75^{NTR}-EGFP (Left) and mut p75^{NTR}-EGFP (Right) constructs, untreated (Top) or treated with proNGF for 30 min (Bottom). Total (green) and surface (magenta) receptor pools are shown, and are quantified in B. EGFP channel levels have been linearly scaled to highlight cone dimensions. (Scale bars, 5 μm.) (D) Timeline of the experiment with Dynasore internalization-inhibiting drug. (E) Dynasore increases the Qdot-to-EGFP ratio even without proNGF, confirming the retention of wt and mut p75^{NTR}-EGFP on the plasma membrane. (F) Retention on the membrane is sufficient for wt p75^{NTR} and mut p75^{NTR} to cause growth cone collapse. Corresponding images are shown in *SI Appendix, Fig. S11A*. ****P* < 0.001, 1-way ANOVA (Tukey’s multiple comparisons). ns, not significant at the 0.05 level. Bars are mean ± SEM. (G) Experimental timeline with Pitstop2 internalization-inhibiting drug. (H) Inhibiting clathrin-dependent internalization causes accumulation of surface p75^{NTR}. ****P* < 0.001, Welch’s test (2-tailed). (I) Retention of p75^{NTR} is sufficient to cause growth collapse without proNGF. ****P* < 0.001, 1-way ANOVA (Bonferroni multiple comparisons). Bars are mean ± SEM. (J) Representative neurons expressing S6-p75^{NTR}-EGFP treated with Pitstop2 or vehicle. Highlighted are extended (empty arrowheads) and collapsed (filled arrowheads) growth cones. Collapsed growth cones show increased surface p75^{NTR} levels, suggesting a cone-autonomous mechanism. (Scale bar, 10 μm.)

were quantified to be a 3/6-fold overestimation in similar ranges of receptor densities (54).

Our dynamics data question the possibility of a covalent TM p75^{NTR} dimerization, challenging a previous model for the p75^{NTR} mechanism of action, which postulates that NT binding to the putative preformed p75^{NTR} covalent dimer induces a conformational change propagated via Cys256, leading to separation of death domains (17). This model was already challenged by structural considerations on the flexibility of the JM and chopper domains (19). We propose an alternative molecular basis for receptor activation, in which p75^{NTR} monomers preferentially concentrate into signaling-competent membrane microdomains, like lipid rafts, upon NGF stimulation, with C256 and G265 residues playing a crucial role in this compartmentalization (Fig. 8A). Indeed, the importance of Cys256 was corroborated by the failure of proBDNF-induced neuronal apoptosis in mut p75^{NTR} knock-in mice (18). This is supported by the observation that wt (but not mut) p75^{NTR} displays higher average residency in GM-1-rich regions upon NGF binding (Fig. 4 E and F), and that the diffusion of NGF-bound wt p75^{NTR} and mut p75^{NTR} displays different responses to cholesterol-modulation treatments (Fig. 4D).

Robust evidence correlates NT signaling, especially proapoptotic signaling, to the residency of NT receptors in lipid rafts,

probably because many interactors and effectors of the pathway are commonly associated with these regions (42, 44, 55). Indeed, p75^{NTR} palmitoylation (Fig. 1C) can mediate the association of the protein with lipid rafts (1), and is necessary for p75^{NTR} proapoptotic activity (27). Hence, p75^{NTR} may be capable of activating apoptosis in these zones only, and lack of proBDNF-induced apoptosis by mut p75^{NTR} (Fig. 5D) can be explained by its inability to enter these regions upon NT binding (Fig. 8A). Our diffusivity data with cholesterol modulation also point to this interpretation (Fig. 4 C–F). It is unclear to us why the modifications of TM residues may impair the residency of p75^{NTR} in lipid rafts. Available models (38) and NMR structures (56) of the p75^{NTR} TM domain agree in not mapping the 2 residues on the same side of the TM helix. We speculate that these residues are involved in creating peculiar interfaces that bind specific lipids (possibly cholesterol itself) or proteic components of lipid rafts; in support of this, cholesterol depletion impaired proBDNF-induced apoptosis (Fig. 5E).

Despite their difference in apoptotic signaling, wt p75^{NTR} and mut p75^{NTR} are equally capable of mediating growth cone collapse in developing neurons (20) (*SI Appendix, Fig. S11A and B*). Here, we showed that this effect is linked to the local concentration of the receptor on the growth cone surface. Although it was previously evaluated in p75^{NTR} overexpression regimes

measure of membrane versus total receptor pool; and 3) for all p75^{NTR} constructs, the intensities in the Qdot channel as a measure of membrane abundance at the different expression levels.

More details on material and methods appear in *SI Appendix*. Readers will be able to access codes and materials by directly contacting the corresponding authors.

ACKNOWLEDGMENTS. We thank Robert Youker for the mut p75^{NTR} construct; Luca Puzzi for the human c-jun complementary DNA, and Gianmichele

Ratto for adeno-associated viral vectors for in vivo YFP expression. We thank Carmine Di Rienzo, Francesco Cardarelli, Marco Canossa, Beatrice Vignoli, Michela Serresi, and Andrea Palamidessi for useful discussions. This study was supported by funding from Tuscany Region, Project NOSEISMIC, within Grant POR CRO FSE 2007-2013 (to S.L.); Ministero Università e Ricerca Projects PRIN 2009XPTWM2 (to S.L.) and FIRB RBAP11X42L (to F. Beltram); Fondazione Pisa Project RST 148/16; European Union Paincage and H2020 Human Brain Projects (SGA1 and SGA2) (to A.C.); and Institutional Scuola Normale Superiore funds (to S.L., L.M., and A.C.).

1. M. Vilar, "Structural characterization of the p75 neurotrophin receptor: A stranger in the TNFR superfamily" in *Vitamins and Hormones*, G Litwack, Ed. (Elsevier, 2017), vol. 104, pp. 57–87.
2. E. J. Huang, L. F. Reichardt, Trk receptors: Roles in neuronal signal transduction. *Annu. Rev. Biochem.* **72**, 609–642 (2003).
3. A. Nykjaer, T. E. Willnow, Sortilin: A receptor to regulate neuronal viability and function. *Trends Neurosci.* **35**, 261–270 (2012).
4. M. V. Chao, Neurotrophins and their receptors: A convergence point for many signalling pathways. *Nat. Rev. Neurosci.* **4**, 299–309 (2003).
5. A. Cattaneo, P. Calissano, Nerve growth factor and Alzheimer's disease: New facts for an old hypothesis. *Mol. Neurobiol.* **46**, 588–604 (2012).
6. X. Q. Chen, M. Sawa, W. C. Mobley, Dysregulation of neurotrophin signaling in the pathogenesis of Alzheimer disease and of Alzheimer disease in Down syndrome. *Free Radic. Biol. Med.* **114**, 52–61 (2018).
7. B. L. Hempstead, D. Martin-Zanca, D. R. Kaplan, L. F. Parada, M. V. Chao, High-affinity NGF binding requires coexpression of the trk proto-oncogene and the low-affinity NGF receptor. *Nature* **350**, 678–683 (1991).
8. T. Wehrman *et al.*, Structural and mechanistic insights into nerve growth factor interactions with the TrkA and p75 receptors. *Neuron* **53**, 25–38 (2007).
9. N. Leloup, L. M. P. Chataigner, B. J. C. Janssen, Structural insights into SorCS2-nerve growth factor complex formation. *Nat. Commun.* **9**, 2979 (2018).
10. P. A. Barker, High affinity not in the vicinity? *Neuron* **53**, 1–4 (2007).
11. X. L. He, K. C. Garcia, Structure of nerve growth factor complexed with the shared neurotrophin receptor p75. *Science* **304**, 870–875 (2004).
12. Y. Gong, P. Cao, H. J. Yu, T. Jiang, Crystal structure of the neurotrophin-3 and p75NTR symmetrical complex. *Nature* **454**, 789–793 (2008).
13. M. Yaar *et al.*, Amyloid beta binds trimers as well as monomers of the 75-kDa neurotrophin receptor and activates receptor signaling. *J. Biol. Chem.* **277**, 7720–7725 (2002).
14. K. C. Wang, J. A. Kim, R. Sivasankaran, R. Segal, Z. He, P75 interacts with the Nogo receptor as a co-receptor for Nogo, MAG and OMgp. *Nature* **420**, 74–78 (2002).
15. J. P. Zanin, E. Abercrombie, W. J. Friedman, Proneurotrophin-3 promotes cell cycle withdrawal of developing cerebellar granule cell progenitors via the p75 neurotrophin receptor. *eLife* **5**, e16654 (2016).
16. C. Langevin, H. Jaaro, S. Bressanelli, M. Fainzilber, C. Tuffereau, Rabies virus glycoprotein (RVG) is a trimeric ligand for the N-terminal cysteine-rich domain of the mammalian p75 neurotrophin receptor. *J. Biol. Chem.* **277**, 37655–37662 (2002).
17. M. Vilar *et al.*, Activation of the p75 neurotrophin receptor through conformational rearrangement of disulphide-linked receptor dimers. *Neuron* **62**, 72–83 (2009).
18. K. Tanaka, C. E. Kelly, K. Y. Goh, K. B. Lim, C. F. Ibáñez, Death domain signaling by disulfide-linked dimers of the p75 neurotrophin receptor mediates neuronal death in the CNS. *J. Neurosci.* **36**, 5587–5595 (2016).
19. K. S. Mineev, S. A. Goncharuk, P. K. Kuzmichev, M. Vilar, A. S. Arseniev, NMR dynamics of transmembrane and intracellular domains of p75NTR in lipid-protein nanodiscs. *Biophys. J.* **109**, 772–782 (2015).
20. A. Anastasia, P. A. Barker, M. V. Chao, B. L. Hempstead, Detection of p75NTR trimers: Implications for receptor stoichiometry and activation. *J. Neurosci.* **35**, 11911–11920 (2015).
21. L. Marchetti *et al.*, Ligand signature in the membrane dynamics of single TrkA receptor molecules. *J. Cell Sci.* **126**, 4445–4456 (2013).
22. T. De Nadai *et al.*, Precursor and mature NGF live tracking: One versus many at a time in the axons. *Sci. Rep.* **6**, 20272 (2016).
23. L. Marchetti *et al.*, Site-specific labeling of neurotrophins and their receptors via short and versatile peptide tags. *PLoS One* **9**, e113708 (2014).
24. F. Gobbo, F. Bonsignore, R. Amodeo, A. Cattaneo, L. Marchetti, Site-specific direct labeling of neurotrophins and their receptors: From biochemistry to advanced imaging applications. *Methods Mol. Biol.* **1727**, 295–314 (2018).
25. A. Callegari *et al.*, Single particle tracking of acyl carrier protein (ACP)-tagged TrkA receptors in PC12nrr5 cells. *J. Neurosci. Methods* **204**, 82–86 (2012).
26. C. Schachtrup *et al.*, Nuclear pore complex remodeling by p75(NTR) cleavage controls TGF- β signaling and astrocyte functions. *Nat. Neurosci.* **18**, 1077–1080 (2015).
27. C. K. Underwood, K. Reid, L. M. May, P. F. Bartlett, E. J. Coulson, Palmitoylation of the C-terminal fragment of p75(NTR) regulates death signaling and is required for subsequent cleavage by gamma-secretase. *Mol. Cell. Neurosci.* **37**, 346–358 (2008).
28. E. Zuccaro *et al.*, Polarized expression of p75(NTR) specifies axons during development and adult neurogenesis. *Cell Rep.* **7**, 138–152 (2014).
29. K. Deinhardt *et al.*, Neuronal growth cone retraction relies on proneurotrophin receptor signaling through Rac. *Sci. Signal.* **4**, ra82 (2011).
30. K. F. Lee *et al.*, Targeted mutation of the gene encoding the low affinity NGF receptor p75 leads to deficits in the peripheral sensory nervous system. *Cell* **69**, 737–749 (1992).
31. C. Costantini, R. Weindruch, G. Della Valle, L. Puglielli, A TrkA-to-p75NTR molecular switch activates amyloid beta-peptide generation during aging. *Biochem. J.* **391**, 59–67 (2005).
32. K. Jaqaman *et al.*, Cytoskeletal control of CD36 diffusion promotes its receptor and signaling function. *Cell* **146**, 593–606 (2011).
33. R. T. Youker *et al.*, Multiple motifs regulate apical sorting of p75 via a mechanism that involves dimerization and higher-order oligomerization. *Mol. Biol. Cell* **24**, 1996–2007 (2013).
34. A. J. Brooks *et al.*, Mechanism of activation of protein kinase JAK2 by the growth hormone receptor. *Science* **344**, 1249783 (2014).
35. I. Chung *et al.*, Spatial control of EGF receptor activation by reversible dimerization on living cells. *Nature* **464**, 783–787 (2010).
36. R. S. Kasai, A. Kusumi, Single-molecule imaging revealed dynamic GPCR dimerization. *Curr. Opin. Cell Biol.* **27**, 78–86 (2014).
37. W. Zhang *et al.*, Single-molecule imaging reveals transforming growth factor- β -induced type II receptor dimerization. *Proc. Natl. Acad. Sci. U.S.A.* **106**, 15679–15683 (2009).
38. A. M. Sykes *et al.*, The effects of transmembrane sequence and dimerization on cleavage of the p75 neurotrophin receptor by γ -secretase. *J. Biol. Chem.* **287**, 43810–43824 (2012).
39. K. Simons, J. L. Sampaio, Membrane organization and lipid rafts. *Cold Spring Harb. Perspect. Biol.* **3**, a004697 (2011).
40. Z. Korade, A. K. Kenworthy, Lipid rafts, cholesterol, and the brain. *Neuropharmacology* **55**, 1265–1273 (2008).
41. F. C. Bronfman, O. M. Lazo, C. Flores, C. A. Escudero, Spatiotemporal intracellular dynamics of neurotrophin and its receptors. Implications for neurotrophin signaling and neuronal function. *Handb. Exp. Pharmacol.* **220**, 33–65 (2015).
42. M. P. J. Dekkers, V. Nikolettou, Y. A. Barde, Cell biology in neuroscience: Death of developing neurons: New insights and implications for connectivity. *J. Cell Biol.* **203**, 385–393 (2013).
43. C. A. Day, A. K. Kenworthy, Tracking microdomain dynamics in cell membranes. *Biochim. Biophys. Acta Biomembr.* **1788**, 245–253 (2009).
44. Y. H. Zhang, R. Khanna, G. D. Nicol, Nerve growth factor/p75 neurotrophin receptor-mediated sensitization of rat sensory neurons depends on membrane cholesterol. *Neuroscience* **248**, 562–570 (2013).
45. C. S. Huang *et al.*, Nerve growth factor signaling in caveolae-like domains at the plasma membrane. *J. Biol. Chem.* **274**, 36707–36714 (1999).
46. F. Pinaud *et al.*, Dynamic partitioning of a glycosyl-phosphatidylinositol-anchored protein in glycosphingolipid-rich microdomains imaged by single-quantum dot tracking. *Traffic* **10**, 691–712 (2009).
47. N. Komura *et al.*, Raft-based interactions of gangliosides with a GPI-anchored receptor. *Nat. Chem. Biol.* **12**, 402–410 (2016).
48. J. M. Frade, A. Rodríguez-Tébar, Y. A. Barde, Induction of cell death by endogenous nerve growth factor through its p75 receptor. *Nature* **383**, 166–168 (1996).
49. S. X. Bamji *et al.*, The p75 neurotrophin receptor mediates neuronal apoptosis and is essential for naturally occurring sympathetic neuron death. *J. Cell Biol.* **140**, 911–923 (1998).
50. M. Zagrebelsky *et al.*, The p75 neurotrophin receptor negatively modulates dendrite complexity and spine density in hippocampal neurons. *J. Neurosci.* **25**, 9989–9999 (2005).
51. L. Cognet, B. Lounis, D. Choquet, Tracking receptors using individual fluorescent and nonfluorescent nanolabels. *Cold Spring Harb. Protoc.* **2014**, 207–213 (2014).
52. T. Yamashita, H. Higuchi, M. Tohyama, The p75 receptor transduces the signal from myelin-associated glycoprotein to Rho. *J. Cell Biol.* **157**, 565–570 (2002).
53. A. K. Lewis *et al.*, Death receptor 5 networks require membrane cholesterol for proper structure and function. *J. Mol. Biol.* **428**, 4843–4855 (2016).
54. P. M. Dijkman *et al.*, Dynamic tuneable G protein-coupled receptor monomer-dimer populations. *Nat. Commun.* **9**, 1710 (2018).
55. P. Mehlen, C. Thibert, Dependence receptors: Between life and death. *Cell. Mol. Life Sci.* **61**, 1854–1866 (2004).
56. K. D. Nadezhdin *et al.*, Structural basis of p75 transmembrane domain dimerization. *J. Biol. Chem.* **291**, 12346–12357 (2016).
57. Y. S. Lim *et al.*, p75(NTR) mediates ephrin-A reverse signaling required for axon repulsion and mapping. *Neuron* **59**, 746–758 (2008).
58. S. Glerup *et al.*, SorCS2 regulates dopaminergic wiring and is processed into an apoptotic two-chain receptor in peripheral glia. *Neuron* **82**, 1074–1087 (2014).
59. N. K. Dhanoa, K. M. Krol, A. Javed, K. A. Crutcher, M. D. Kawaja, Null mutations for exon III and exon IV of the p75 neurotrophin receptor gene enhance sympathetic sprouting in response to elevated levels of nerve growth factor in transgenic mice. *Exp. Neurol.* **198**, 416–426 (2006).
60. E. E. Zahavi *et al.*, The receptor tyrosine kinase TrkB signals without dimerization at the plasma membrane. *Sci. Signal.* **11**, ea04006 (2018).
61. S. Covaceuszach *et al.*, The conundrum of the high-affinity NGF binding site formation unveiled? *Biophys. J.* **108**, 687–697 (2015).

Supplementary Material and Methods

Expression constructs

S6-tagged human wild-type p75^{NTR} (wt p75^{NTR}) construct was previously described (1). In this study we used S6- wt p75^{NTR} cloned both as C-terminal GFP fusion in pReceiver-M03 (GeneCopeia™), and without GFP in an “all-in-one” third generation Tet-on lentiviral pTRE vector. In the first case, expression is driven by CMV promoter, in the second one by an inducible promoter bearing a Tet-responsive element (TRE) (2). Mutated p75^{NTR} (mut p75^{NTR}), bearing deletion corresponding to 221-246 aminoacids (193-218 in previous nomenclature (3)) plus C256A and G265I point mutations in pEGFP-N1 (Clontech) was a gift from Dr. Robert Youker and was subjected to insertional mutagenesis to introduce S6 tag (1) and either used as is, or subcloned in lentiviral pTRE vector. S6-tagged p75^{NTR}-LeucineZipper chimera construct (dim p75^{NTR}) was generated from tagged wt p75^{NTR} by replacing a region encompassing its juxtamembrane domain (206-251 aminoacids) with the leucine zipper (LZ) motif of human c-Jun, cloned in pCDNA3.1 (Life Technologies) and either used as is, or subcloned in lentiviral pTRE vector. S6-tagged wt TrkA construct was previously described (1). pTagRFP-actin and pTagRFP-Lamin are from Evrogen. wt Dynamin1-pmCherryN1 (Addgene 27697) and Dynamin1(K44A)-mRFP (Addgene 55795) were already described (4, 5). Soluble GFP used in this study is pEGFP-N1 plasmid from Clontech or EGFP cloned in pTRE lentiviral vector. Farnesyl-GFP construct was described previously (6). All primer sequences used in cloning procedures are reported in Table S2.

Cell culture

SH-SY5Y (ECACC 94030304), SK-N-BE(2) (ATCC® CRL-2271™), CHO-K1 (ATCC® CCL-61™) cell lines were grown in DMEM/F-12 medium supplemented with 10% Fetal Bovine Serum, 1% Penicillin-Streptomycin, 1% L-Glutamine and 25 mM HEPES. HEK293T/17 (ATCC® CRL-11268™) cell line was grown in DMEM High-Glucose (4.5 g/L D-Glucose) medium supplemented with 10% Fetal Bovine Serum, 1% Penicillin-Streptomycin, 1% L-Glutamine and 1% Sodium Pyruvate. PC12 cell line was grown in RPMI1640 medium supplemented with 10% Horse Serum, 5% Fetal Bovine Serum, 1% Penicillin-Streptomycin, 1% L-Glutamine. Hippocampal and brain cortex tissues were extracted from wild-type (B6129) or p75 knockout (7) P0-P4 mice; the procedure was approved by the Italian Ministry of Health and was conducted in compliance with the Italian National Research Council guidelines. Primary neuron (P0) or astrocyte (P4) cultures were established as described in (8). The day of plating was defined as day-in-vitro (DIV) 0. After surgery and isolation, hippocampus and cortex tissues were grinded up in cold Ca²⁺-free Hank's Balanced Salt Solution (HBSS) (Sigma-Aldrich®), supplemented with 1% Penicillin-Streptomycin. 0.1% trypsin and 100 U/ml DNase (Sigma-Aldrich®) were then added for digestion. Following trypsin inactivation in 10% FBS DMEM, neurons were seeded on plasma-treated WillCo® dishes or glass slides, previously coated with Poly-D-lysine (PDL), in Neurobasal-A medium (Gibco) supplemented with 4.5 g/L D-Glucose (Sigma-Aldrich®), 10% FBS, 2% B-27 (Gibco), 1% GlutaMAX (ThermoFisher), 1 mM sodium pyruvate, 4 μM reduced glutathione (Sigma-Aldrich®), 12.5 μM glutamate (Sigma-Aldrich®). From DIV 1 on, neurons were maintained in Neurobasal-A supplemented with 2% B-27, 1% GlutaMAX, 1-10 μg/ml Gentamicin (culture medium) and medium was refreshed every 2-3 days. In all our assays except those shown in Fig. 6a, DIV 3 neurons were used. Astrocytes cultures were established by seeding dissociated cells on previously PDL coated flasks in DMEM/F-12 medium supplemented with 10% Fetal Bovine Serum, 1% Penicillin-Streptomycin and 1% L-Glutamine and 25 mM HEPES as described in (9). In our experiments we used mature (two- to three-week-old) astrocytes, obtained by trypsinization of the flasks and seeding on Poly-D-lysine coated WillCo® dishes. All cell cultures were maintained at 37°C, 5% CO₂ in a humidified incubator.

Acyl-Biotinyl Exchange (ABE) Assay

The ABE assay was performed as previously described (10), with modifications. Briefly, SH-SY5Y cells were transfected with S6-wt p75^{NTR} (pTRE plasmid) and, after 24 hours induced with 1 μg/ml doxycycline, washed twice with ice-cold PBS and lysed in RIPA Buffer supplemented with 10 mM N-Ethylmaleimide (NEM), 2x Protease Inhibitors (a fresh 100x stock was made by 1 mg/ml of Pepstatin and 10 mg/ml of each Leupeptin, Antipain and Chymostatin, and then 50-fold diluted) and 2 mM Phenylmethylsulfonyl fluoride (PMSF) on ice. Cells lysate was transferred in 1.5 ml tubes and end-over-end rotated for 1 hour at 4°C. The solution was then centrifuged for 30 min, 4°C, 16000 ×g and protein concentration was determined by Pierce™ Coomassie (Bradford) Protein Assay Kit (ThermoFisher Scientific). Half of the sample was treated with 0.7 M Hydroxylamine (HA) and half was not (as a control, -HA), then both were supplemented with 0.2 mM N-[6-(Biotinamido)hexyl]-3'-(2'-pyridyldithio)propionamide (HPDP-biotin, ThermoFisher Scientific). Differently from (8), the biotinylated pool from +HA and -HA samples was then precipitated with Dynabeads® MyOne™ Streptavidin C1 (ThermoFisher Scientific) and the supernatant (SPN +HA and SPN -HA) kept as a control. Complexes of streptavidin beads and biotinylated proteins were washed twice with PBS supplemented with 0.02% Tween®20. The beads were heated at 95°C for 10 minutes in SDS gel loading buffer 2x (20% glycerol, 4% sodium dodecyl sulfate, 0.1 % bromophenol blue, 100 mM Tris-HCl pH 6.8, 5% β-mercaptoethanol); eluted proteins were loaded on a 4–12% Criterion™ XT Bis-Tris Protein Gel (Bio-Rad) and then transferred to a nitrocellulose membrane and blotted with anti P75^{NTR} antibody (07-476, Millipore) 1:1000 diluted in TBST (150 mM NaCl, 20 mM Tris HCl pH 7.4, 0.05% Tween®20) plus 5% Non-Fat Dry Milk (Bio-Rad). All reagents were purchased from Sigma-Aldrich except where otherwise stated.

p75^{NTR} constructs expression, localization and S6 tag labeling

p75^{NTR} constructs were expressed in cells by means of transfection with Lipofectamine 2000 (Thermo Fisher Scientific) according to the manufacturer instructions, or they were transduced using inducible third-generation lentiviral vectors. In the latter case, packaging in HEK293T cells and concentration with Lenti-XTM Concentrator (Clontech) was performed as described (2). To assess the correct membrane localization of S6-tagged wt p75^{NTR}, we lipofected it in SH-SY5Y; cells were then seeded on glass-bottomed dishes and, after 24 hours, imaged with confocal SP2. As a reference, we observed subcellular distribution of endogenous p75^{NTR} in PC12 cells transfected with pTagRFP-lamin or farnesyl-GFP and immunostained, the next day, with an anti p75^{NTR} antibody (07-476, Millipore). Samples were then imaged with confocal SP2, using a laser diode with 403 nm excitation wavelength and [410-470] nm emission window for Hoechst (added to the medium immediately before imaging); for EGFP we exploited the 488 nm line of the Argon laser with [500-550] nm emission window. Colocalization of native p75^{NTR} was verified by overlapping the intensity (I) versus distance (d) plots of line profiles, drawn in the two channels with ImageJ software.

SH-SY5Y, SK-N-BE(2), CHO-K1, HEK293T/17, astrocytes and neurons, in their related culture medium, were transduced with viral like particles containing the three p75^{NTR} constructs. To reach optimal p75^{NTR} expression, doxycycline was added to the culture medium for at least 18-24 hours before every experiment. We calibrated doxycycline doses to get the most suitable receptor level for each type of assay, also considering that the same receptor level was reached at different doxycycline doses in different cellular models. For single molecule experiments in neuroblastoma cell lines, 0.001 – 0.01 µg/ml doxycycline range was used to get wt and mut p75^{NTR} low (< 0.18 receptors/µm²), medium (0.18 < receptors/µm² < 0.36) and high (> 0.36 receptors/µm²) membrane receptor densities; dim p75^{NTR} was also transduced but we only got low densities in this case, therefore we also transfected the corresponding construct in pCDNA3.1, and observed it at least 24 hours later, in order to explore medium-high density ranges. Cells in the medium density range were used for the tracking analysis, while for the single-step photobleach analysis we also used cells in the high range (up to 0.5 receptors/µm²) upon induction with 0.05 µg/ml doxycycline. For experiments with neurons, we found 0.05 µg/ml doxycycline to be optimal, as lower concentrations were not sufficient to reach medium-high membrane p75^{NTR} densities in the tracking experiments (Fig. S7); also, this doxycycline concentration, but not higher concentrations like 1 µg/ml, ensured reliable results in the cleaved caspase-3 assay (compare Fig. 5 and Fig. S9). After induction or transfection, cells were labeled as stated in (2). Briefly, cells were washed once with PBS and labeled with one of these strategies: i) for one-color and dual-color single molecule experiments we prepared a mix containing 2 µM Sfp Synthase, 10 mM MgCl₂, 5 - 10 nM of a CoA-conjugated form of Abberior635P in culture medium; ii) for growth cone collapse assay and p75^{NTR} polarized localization in neurons we prepared this mix: 2 µM Sfp Synthase, 10 mM MgCl₂, 10 µM CoA-biotin in culture medium. Both were added to cells for 30 min at 37°C. After ii), cells were washed three times with PBS and subjected to a second reaction with 10 nM S-Qdot655 in Qdot Binding Buffer (borate buffer pH 8.3, supplemented with 0.5% BSA and 215 mM sucrose) for 2 min at room temperature, washed again five times with PBS and imaged; instead, after i) cells were washed five times with PBS and imaged.

Preparation of recombinant neurotrophins

Preparation of hproNGF and hNGF procedure has been already published (11). For preparation of hproBDNF, the hproBDNF cDNA was subcloned in the prokaryotic expression vector pET11a and the protein was expressed as recombinant protein in *E. coli* strain BL21(DE3), refolded from inclusion bodies and purified by using protocols adapted from previously published ones (12, 13). Briefly, BL21(DE3) *E. coli* were transformed with 30 ng of plasmid pET11a containing the gene of human proBDNF; bacteria were plated on Luria-Bertani (LB) agar plates supplemented with Ampicillin (Amp) and grown overnight at 37°C. Then a single colony was inoculated in 20 ml of LB supplemented with Amp and grown overnight at 37°C with shaking at 250 rpm. The day after, the inoculum was diluted 1:50 in 1L of LB + Amp and grown at 37°C at 250 rpm to reach an OD600 of about 1 before induction with 1 mM of isopropyl-b-thiogalactoside (IPTG). The proBDNF production was continued at 37°C at 250 rpm shaking. After 5 hours bacteria were collected by centrifugation at 5,000 × g for 10 min at 4°C. The bacterial pellet was first resuspended with Lysis Buffer (10 mM TRIS HCl pH 8, 1 mM EDTA and 1mg/ml lysozyme) at 5 ml/g v/w ratio and incubated at room temperature for 1 h. After sonication on ice (3 cycles of 45 seconds on and 60 seconds off using a MicrosonTM Ultrasonic Cell Disruptor XL at maximum power), 3 mM MgCl₂ and 50 µg/ml DNaseI solutions were added and the sample was incubated at room temperature for 30 minutes. To isolate inclusion bodies (IBs), 0.5 vol. of Triton Buffer (60 mM EDTA, 1.5 M NaCl, 6% Triton X-100) was added and the sample was incubated at room temperature for 30 minutes on a stirring plate. The IBs were then centrifuged at 18000 × g for 30 minutes at 4°C, resuspended in 20 ml of resuspension buffer (10 mM TRIS HCl pH 8, 1 mM EDTA) 0.5 vol. of Triton Buffer and incubated at room temperature for 30 minutes on a stirring plate. The IBs were then centrifuged at 18000 × g for 30 minutes at 4°C and subsequently washed three times with a total volume of 100ml of Washing Buffer (50 mM TRIS HCl pH 7.5, 1 mM EDTA). The IBs pellet was then resuspended with 5 ml/g of Solubilization Buffer (6M guanidinium, 100 mM TRIS HCl pH 8, 1 mM EDTA and 100 mM DTT), and incubated until complete solubilization at room temperature on a rocking plate. Then the pH was lowered to 3.5 with HCl 3M and the sample was centrifuged at 18000 × g for 30 minutes at 4°C. The resulting solution was dialyzed three times against 300 ml of Dialysis Buffer (6M guanidinium pH 3.5) each one for twelve hours using Visking dialysis membrane (cut-off 7 kDa, Medicell Membranes Ltd) and the protein concentration was measured with the Bio-Rad Protein Assay. IBs solution containing denatured hproBDNF was refolded by a drop by drop addition in 100 ml of Refolding buffer (1 M Arginin, 100 mM TRIS HCl pH 9.3, 5 mM EDTA pH 8, 1mM GSSG and 5 mM GSH). Every hour 50 µg/ml of sample were added

to the buffer under vigorous stirring at 4 °C. After 16-48 hours the sample was dialyzed at 4 °C using a Visking dialysis membrane (cut-off 12-14 kDa, Medicell Membranes Ltd) against 2 L of IEX-A (50 mM Na phosphate pH 7, 1 mM EDTA) replacing the buffer after 12 hours. The dialyzed sample containing proBDNF was filtered using a 0.22 µm filter and purified by FPLC. The sample was loaded on a HiLoad 16/10 SP Sepharose High Performance (~20 ml - GE Healthcare) equilibrated with IEX-A buffer using a liquid chromatography system (ÄKTA™ - FPLC). The protein was eluted with linear gradient from 0 to 100% of IEX-B (50 mM Na phosphate pH 7, 1 mM EDTA and 1M NaCl) at 1ml/min flow in 6 column volume (CV) and 2ml fractions collected. The ones corresponding to the UV(280nm) FPLC peak containing hproBDNF were pooled and dialyzed against 100 mM Hepes pH 7.5, 1 mM CaCl₂. The dialyzed protein was concentrated up to 1mg/ml using an Amicon ultrafiltration membrane with 10 kDa cut-off (Merck-Millipore) and stored at - 80 °C. The purity and the correct molecular weight of the protein was monitored by SDS-PAGE and MS analyses.

Cell cholesterol-content modulation and quantification

In order to modulate membrane cholesterol levels of SK-N-BE(2) cells, these were treated as follows: i) 10 µM mevastatin overnight treatment to decrease cholesterol content ii) 5 mM of cholesterol:MβCD plus 5 µM of free cholesterol incubated for 30 min at 37°C to increase cholesterol content.

In order to modulate cholesterol levels in neurons for the proBDNF apoptosis assay, cholesterol biosynthesis was inhibited with 10 µM mevastatin for 50 h starting on DIV 2; on DIV 3, neurons were treated for 30 min with 5mM of Methyl-β-cyclodextrin, washed three times and incubated for 12 hours with 10 µM mevastatin, with or without 20 ng/ml proBDNF. To increase cholesterol content, 5 mM of cholesterol:MβCD plus 5 µM of free cholesterol were added to the proBDNF or control mixes for the first 30 minutes of the 12h incubation on DIV 3 neurons. After 30 minutes, this medium was washed three times and changed into normal medium with (or without) proBDNF. To assess membrane cholesterol levels, cells were seeded on Willco® dishes, cultured and washed twice with PBS and stained with fluorescent filipin III of Cholesterol Assay Kit (Cell-Based) (Abcam) following manufacturer guidelines. Stained samples were imaged at TIRF microscope with HCX PL APO 100.0X oil-immersion objective, using a 405 nm laser with a Quad ET TIRF MC fluorescence cube, a [420 - 510] nm emission filter and a 90 nm penetration depth. Typically, a 272 x 320 pixels (61.94 x 72.91 µm) field was analyzed by ImageJ software, measuring filipin mean intensity of the whole field after background subtraction and application of a threshold to remove pixels outside the cells. For filipin intensity quantification in neurons, glia signal was always removed from the image before measurement; furthermore, samples treated with cholesterol-affecting drugs -due to loss of glass-adhered neuronal plasma membrane caused by the treatment- were not imaged at TIRF, but at confocal SP2 using HCX PL APO CS 40.0X oil-immersion objective (NA 1.25), a 378 nm laser line, and [390 - 470] nm emission. 512 x 512 pixels (124.97 x 124.97 µm) fields were acquired and quantified measuring filipin III mean intensity of each neuron after background subtraction.

Microscopy setups

Cell imaging was performed by both confocal and TIRF microscopy. In the first case, we used Leica TCS SP2 on inverted DM IRE2 with HCX PL APO CS 63.0X oil-immersion objective (NA 1.40), and Argon and diode lasers, with pinhole set at Airy 1 [confocal SP2]; or Leica TCS SP5 on DM6000 confocal microscopes with Argon and various solid-state lasers [confocal SP5] (Leica Microsystems). Objectives and pinhole values have been changed depending on the experimental requirements, as indicated in the following or in the specific experiment description. For growth cone collapse assay, we used oil objective HCX PL APO CS 40.0X (NA 1.25) and pinhole at 1 Airy Unit. Ar 488 nm laser line was used for EGFP ([500-550] nm emission window) and S-Qdot655 ([650-750] nm emission window), a solid-state 561 nm laser for TagRFP ([575-650] nm emission range) and a pulsed 405 nm laser for DAPI ([420-500] emission range).

For cleaved Caspase-3 assay, we used HC PL FLUOTAR 20.0X air-objective (NA 0.5) and pinhole at 1.5 Airy Units, a 633 nm laser line and [648-718] nm emission window for Alexa647, a 488 nm laser and [500-600] nm emission window for Alexa488 and a pulsed 405 nm laser line with [410-500] nm emission range for DAPI. For axon morphology analysis we used a HCX PL APO CS 40.0X objective; excitation laser lines and collected emitted fluorescence were 488 nm and [500-550] nm for EGFP, 561 nm and [575-650] nm for TagRFP-actin, and 633 nm and [650-750] nm for Alexa647.

For TIRF microscopy, we used Leica DM6000 inverted microscope (Leica Microsystems) equipped with epifluorescence module, DIC in transmission, TIRF-AM module operating in one-color or dual-color modes, HCX PL APO 100.0X oil-immersion objective (NA1.47), and four laser lines. For TIRF single-color measurements, we used an EM-CCD camera (ImagEM C9100-13, Hamamatsu) on the bottom port, after a -0.7x adapter and filter mounter, obtaining image pixel dimensions of 228 nm (unless the use of a 1.6x or a 2x magnifier is stated, in which case pixel dimensions are 143 and 114 nm, respectively). Unless otherwise stated, we used the "Hamamatsu overlapping mode" in the Leica AF6000 software and collected data from a rectangular ROI on the CCD, obtaining a frame time equal to the integration time. For TIRF dual-color mode, we used an external laser combiner (iFLEX-adder, QiOptiq), using kineFLEX polarization maintaining fibers (QiOptiq) and kineMATIX fiber coupler (QiOptiq), and a 488nm supplementary laser (iFLEX-iRIS, QiOptiq) with power tuned by a DAC. The used fluorescence cube contained the TRF59906 - ET - 488/640nm Laser Dual Band Set for TIRF applications (Chroma). Typically, laser powers at the objective were set at 0.178 mW (488 line) and 2.6 mW (635 line of the Leica system); the penetration depth was set at 130 nm for the 635 nm laser line corresponding to a penetration depth of about 100 nm for the 488 nm line. To detect both channels at the same time, a Dual View (Optical Insights DV-CC, with filters Chroma ET525-50 and r647lp and dichroic beam splitter T600lpxr) was placed in front of

an EM-CCD camera (iXon Ultra 897, Andor) on the left port, so that emitted light was splitted and collected in the two halves of the camera. We included an Optomask adjustable field mask (OPTMSK-L, Andor) between the microscope output and the DualView in order to limit illuminated area of the camera and increase the frame rate. Camera parameters were optimized to achieve the best compromise between temporal resolution and signal-to-noise ratio: temperature was set to -75°C , pixel clocking rate to 17000 MHz, vertical shift speed to $0.5\ \mu\text{s}$, and vertical clock voltage to +2. The DualView windows in the different channels were aligned for tilting, horizontal position, and correspondence of imaged areas using bright field imaging of the supplied grid, taking care of leaving ~ 3 unilluminated pixels between the two. A constant ROI of 343×127 pixels ($54.72 \times 20.16\ \mu\text{m}$, corresponding to $\sim 27.2 \times 20.16\ \mu\text{m}$ for each single color window, having image pixel sizes of 160nm) was used to acquire 500-frame time series with integration time of 21 ms and frame time of 30 ms. All microscopes were equipped with incubator chambers to maintain 37°C , 5% CO_2 conditions for live cell imaging. More details can be in each specific experiment description.

One-color single-molecule p75^{NTR} imaging and tracking

In order to test whether S6 tag affects polarization of p75^{NTR} in neurons, we infected DIV1 hippocampal neurons with wt p75^{NTR} and soluble EGFP lentiviral particles. After labeling with S-Qdot655, cells were imaged by TIRF microscopy with a 488 nm excitation laser, a Qdot655 emission filter (FF01-655/15 Semrock) and a penetration depth of 110 nm. A constant region of interest (ROI) of 232×240 pixels ($52.80 \times 54.63\ \mu\text{m}$) was used to acquire 500-frame time series with integration time of 47 ms, and the trajectories of the single-membrane receptors were reconstructed as specified below. Relative enrichment of p75^{NTR} was calculated as the ratio between the percentage of the area of neurites and somas explored by S6- p75^{NTR} trajectories. Neurite and soma ROIs were hand-drawn on DIC image, and the area explored by p75^{NTR} was calculated using a custom macro in ImageJ, that counts the number of pixels containing the coordinates of at least one spot throughout all trajectories of a movie.

For single molecule dynamics experiments, cells transduced with S6-tagged p75^{NTR} constructs were labeled with Abberior 635P and usually imaged within 30 minutes after labelling. Cholesterol affecting treatments were performed before (mevastatin) and during (cholesterol load) the labeling reaction. Ligand stimulation was performed by addition, into the medium of the labelled cells, of NGF (150 ng/ml) or its immature form (300 ng/ml proNGF). In this experiment, p75^{NTR} dynamics was monitored for a total of 15 minutes after ligand administration to culture medium. Samples were imaged at the TIRF microscope, using a 635 nm excitation laser, a Cy5 Leica 152303 emission filter and a 110 nm penetration depth. Usually a 500-frame time series was acquired in a fixed 200×208 pixels ($45.49 \times 47.31\ \mu\text{m}$) ROI, with 21 ms integration time for movies acquired at 228 nm pixel size and 30 ms integration time for movies acquired at 143 nm pixel size. For analysis on single particle movies, we developed algorithms in MATLAB R2015b (The MathWorks, Inc.). The analysis was based on the work presented in (14) (refer to this reference for some details not reported here), but using functionalities from the u-track 2.1.3 software (Danuser Lab) (15) for detection, localization, and tracking of spots. In order to automatize as much as possible this part of the analysis, we integrated in our algorithms these procedures, together with automatic file loading using the OME Bio-Format package, revision 33bb1150. Briefly, we applied a mask to movies from one-color experiments in order to exclude spots outside of cell membranes due to fluorophores unspecifically adhered to the glass; this operation was done either with ImageJ software or with a home-made algorithm, starting from a maximum intensity projection of the whole movie. The detection of the spots was made with a custom-modified u-track algorithm, where particles recognition at the borders of the mask was optimized, since we observed often misdetection or undetection. Particles positions were detected in xy over time and the correspondent trajectories were generated as standard in the u-track software. The output trajectories can be composed by several subtrajectories, linked to each-other in order to take into account merge and/or split events (M&S events), where two spots can associate or dissociate. Therefore, there are actually part of trajectories where more than one molecule travel together. We developed an algorithm to separate all the subtrajectories composed by a different numbers Np of particles, obtaining therefore only non-branched trajectories. Used additional outputs of this procedure are the total number of M&S events in a movie, and Np for each subtrajectory (actually, an estimate for a minimum number of particles in a subtrajectory considering only M&S events). Transient dimer (Td) subtrajectories are the ones with $Np=2$ preceded by a merge event and followed by a split event; we retrieved their number and the average and standard error of their duration distribution per cell, and used these data to obtain the total distributions in Fig. 2g (as in (14)). From all subtrajectories, two main parameters were calculated as in (14): average intensity (I_{av}), which is the average of the intensities of the spots (given by the u-track algorithm) in the whole track, and D , which is the diffusion coefficient calculated on the first two points of the Mean Square Displacement (MSD) function. Their distributions have been calculated like in (14), taking into account their uncertainty and the number of frames when the particle has been detected in a trajectory. It should be noted that the D values calculated for many of the trajectories contributing to the D distributions below $\sim 0.1\ \mu\text{m}^2/\text{s}$ are compatible with $0\ \mu\text{m}^2/\text{s}$ when considering the uncertainties. Thus, we do not exclude that the low tail of slowly diffusing trajectories visible in the D distribution (Figs. 2d, S8c) may correspond to immobile or much slower fluorophores. Finally, we also calculated for each cell the spot density, which corresponds to the average number of detected spots (excluding those not belonging to a track) in the first 5 frames of the movie divided by the area of the cell bottom membrane.

Stoichiometry by single-molecule step photobleaching

For step-photobleaching quantification, we used the three p75^{NTR} constructs above described plus the S6-tagged TrkA construct (1) transduced in SK-N-BE(2) cells and labeled with 20nM CoA-Abberior635P for 30 min at 37°C according to (2). TrkA expressing cells were treated for 15 min at 37°C with 125 ng/ml mouse NGF (Alomone Labs), diluted in medium without serum. After that, both p75^{NTR} and TrkA samples were fixed for 90 min at room temperature with 4% PFA/Sucrose solution supplemented with 0.1% Glutaraldehyde (GA, Electron Microscopy Sciences) (16), washed five times with PBS and imaged in PBS at the TIRF microscope. We employed the same microscope setup used for single molecule dynamics experiment, but for a 3000-frame movie (needed to achieve exhaustive fluorophore photobleaching) acquired in a 144 x 144 pixels (32.68 x 32.68 μm) ROI, with 21 ms integration time. We acquired time series of about 60 sec, reaching at least 80% dye photobleaching. Time series were then analyzed as described previously (17). Briefly, background fluorescence was subtracted using the ImageJ software rolling ball algorithm (with a 6 pixel radius) on the whole movie. The first 20 frames were averaged, and a mask was calculated on this image using a threshold lower bound set as four times the mean intensity of a region without fluorescent spots; such mask was then applied to the whole movie. Single spots were selected on the first frame of the background-subtracted and thresholded TIRF movie using a 3 x 3 pixels ROI, their intensity profile during time was plotted and we quantified the number of photobleaching steps and the pre-bleach mean intensity. Precise criteria were applied to select particles: i) spots needed to be clearly distinguishable and not belonging to areas of clustered receptors; ii) number of photobleaching steps was calculated only for profiles whose intensity reached background by the end of the movie; the others were used only to calculate the pre-bleach mean intensity; iii) spots whose intensity step up during the movie were discarded; iv) spots whose intensity profiles were very scattered were discarded; v) the first photobleaching step must be at least 5 frames long; vi) when blinking occurs, pre-blink intensity must be equal to post blink one; vii) blinking must in any case not exceed 20% of the time the particle is observed; viii) when more than one photobleaching events are observed, their relative steps must be similar. For the selected spots, we plotted the intensity profile and quantified the number of photobleaching steps and the pre-bleach mean intensity. The frequency distribution of pre-bleach intensity was fitted with a multi-gaussian function: we assumed linear summation of mean and variance, yielding the following equation:

$$\frac{A_1}{\sigma} \cdot e^{-\frac{(x-x_c)^2}{2\sigma^2}} + \frac{A_2}{\sigma\sqrt{2}} \cdot e^{-\frac{(x-2x_c)^2}{4\sigma^2}} + \frac{A_3}{\sigma\sqrt{3}} \cdot e^{-\frac{(x-3x_c)^2}{6\sigma^2}} + \frac{A_4}{2\sigma} \cdot e^{-\frac{(x-4x_c)^2}{8\sigma^2}},$$

where x_c is the mean value of the first peak and σ^2 is its variance. A_1 , A_2 , A_3 and A_4 are multiplying factors that represent how populated each species is.

Dual-color lipid raft and p75^{NTR} imaging

SK-N-BE cells infected with S6-tagged wt or mut p75^{NTR} were seeded on Willco® dishes and expression induced with 0.01 μg/ml doxycycline. p75^{NTR} was labeled with CoA-Abberior635P, treated with fresh medium or 100 ng/ml human NGF in fresh medium for 15 min at 37°C and subjected to lipid raft staining by means of Vybrant Alexa Fluor 488 Lipid Raft Labeling Kit (ThermoFisher Scientific). Briefly, cells were labeled with Cholera Toxin-subunit B (CT-B) conjugated with Alexa488, washed five times with cold PBS, crosslinked with Anti-CT-B, washed again five times with cold PBS and imaged. All of the rafts staining steps were performed at 4°C in medium with or without NGF. Samples were then imaged at 37°C either in absence or presence of NGF, using the TIRF microscope in the two-color configuration: Abberior635p was excited at 635 nm (red channel) and Alexa488 at 488 nm (green channel). Misalignments between the green (raft) and red (p75^{NTR}) channels can remain after the alignment procedure for the Dual View, also because of chromatic aberrations; these were corrected using a superposition algorithm. This was implemented (i) acquiring a DIC image immediately before or after the fluorescence time-lapse; (ii) extracting from the DIC images and movies the “green” and “red” windows excluding the pixels on the borders; (iii) finding the best affine transformation for superimposing the DIC “green” channel on the corresponding “red” one using the ‘imregtform’ function in MatLab; if this transformation could not be found, or if the Pearson correlation coefficient for the superposition of the transformed green image on the red one was less than 0.85, the best transformation found for the series of experiments (on the same petri) was used instead; (iv) transforming the green fluorescence movie using the ‘imwarp’ function in MatLab with the transformation found in point iii and ‘cubic’ interpolation. The localization of p75^{NTR} spots in raft or non-raft regions was quantified using the ratio of the average intensity of the red channel (p75^{NTR}) inside the raft (green-positive) regions ($\bar{I}_{raftp75}$), divided by the average intensity of the red channel in the whole cell ($\bar{I}_{totalp75}$); this parameter is analogous to the first Manders split coefficient, but corrected for the area of raft and non-raft regions. To evaluate green-positive regions, we applied an image segmentation algorithm to the whole movie, treated as a 3D image; the segmentation was based on a seed-and-threshold method (<https://svi.nl/SeedAndThreshold>), but with two sets of thresholds (as percentages over the maximum intensity in the green channel) for high-intensity and low-intensity regions.

Axon morphology analysis

Dissected hippocampal neurons from wt or p75^{NTR} KO mice were cultured at low density and on DIV 1, transfected with Lipofectamine 2000 (Thermo Fisher) with soluble EGFP and pTagRFP-actin following manufacturer’s instruction. On DIV 5, neurons were fixed in 4% formaldehyde 5% sucrose PBS and permeabilized for 7’ in 0.1% Triton X-100 PBS 2.5% BSA. After 5 washes in PBS, samples were blocked in 5% BSA/PBS and incubated for 2 hr at room temperature with 1:500 anti-NFH200 (abcam ab7795) in 2.5% BSA/PBS, followed by 1:100 anti-mouse Alexa647 (ThermoFisher Scientific). Samples were mounted with Fluoroshield with DAPI and imaged at confocal SP5 using HCX PL APO CS

40.0X objective. Excitation laser lines and collected emitted fluorescence were 488 nm and [500-550] nm for EGFP, 561 nm and [575-650] nm for TagRFP-actin, and 633 nm and [650-750] nm for Alexa647. In rescue experiments, neurons from p75^{NTR} KO mice were transfected on DIV 1 with S6-tagged wt or mut p75^{NTR}-EGFP, and pTagRFP-actin, and fixed and processed for immunofluorescence on DIV 5. Axons were identified as NFH-200 immunoreactive protrusions and analyzed using ImageJ. Axon length was measured as total linear axon length. Branch points were counted as axon bifurcations whose emerging branches were at least 10 μ m in length. Lateral growth cones are actin-positive growth cones emerging along the axon and not disposed terminally.

Growth cone collapse assay

DIV1-2 hippocampal neurons were transiently transfected with S6-wt-p75^{NTR}-GFP or S6-mut-p75^{NTR}-GFP using Lipofectamine2000 (Thermo Fisher); alternatively, they were transduced with inducible lentiviral vectors bearing S6-wt-p75^{NTR} or S6-mut-p75^{NTR} according to an established procedure (2). Control cultures were transfected or transduced with soluble EGFP. To help growth cone area evaluation, cultures were co-transfected with pTagRFP-actin, or subjected to phalloidin staining (Thermo Fisher) after cell fixation. To evaluate the role of p75^{NTR} internalization in growth cone collapse, cultures were co-transfected with a red fluorescent wt- or K44A- Dynamin 1 construct. For inducible p75^{NTR} expression, we added 0, 0.05 or 1 μ g/ml doxycycline to the neuron growth medium after infection. On DIV3, fresh medium was added to control neurons, while p75^{NTR} expressing ones were incubated with the following labeling mix in fresh medium: 2 μ M Sfp Synthase (New England Biolabs), 10 mM MgCl₂, 10 μ M CoA-biotin for 30-45 min at 37°C, in order to biotinylate S6-tags exposed at the cell surface. All neurons were then washed three times with HBSS (supplemented with 2mM CaCl₂ and 1 mM MgCl₂) and incubated 30 minutes at 37°C with either culture medium only or 20 ng/ml proNGF in culture medium. Neurons were then washed once; p75^{NTR} expressing neurons were incubated with 10 nM Qdot™ 655 Streptavidin Conjugate (S-Qdot655, ThermoFisher Scientific) for 15 min at 4°C, then washed 5 times and fixed in 2% formaldehyde plus 5% Sucrose in PBS for 15 min at room temperature, washed three times with PBS and imaged. To inhibit dynamin-dependent endocytosis, the above experiment was repeated in the presence of 80 μ M Dynasore (Sigma-Aldrich) in the biotinylation step and proNGF (or control) treatment. To selectively inhibit clathrin-dependent endocytosis, the experiment was also repeated with addition of 25 μ M Pitstop2 (Abcam, ab120687) only during proNGF treatment, or with 0.5% DMSO as a control. Imaging was done with confocal SP5, using oil objective HCX PL APO CS 40.0X (NA 1.25) and the pinhole set at 1 Airy Unit. A 488 nm laser line was used for EGFP ([500-550] nm emission window) and S-Qdot655 ([650-750] nm emission window), a solid-state 561 nm laser for TagRFP ([575-650] nm emission range) and a pulsed 405 nm laser for DAPI ([420-500] emission range). Alternatively, we used the TIRF microscope in epifluorescence mode, using oil objective 100.0X (NA 1.47) and a 2x magnifier lens. Images of Qdot655 labelled receptors were acquired using a 488nm laser line and FF01-655/15 Semrock emission filter; RFP or mCherry were imaged using the 561nm laser line and a Cy3 filter cube; GFP or Phalloidin-Alexa488 were imaged using a 488nm laser line, a 482-510 excitation filter and a BP 525/20 Leica emission filter. For each experiment, we quantified with ImageJ software from background-subtracted images: i) the area of all detectable growth cones, as derived from the RFP-actin, GFP or Phalloidin channels; ii) for S6-p75^{NTR}-EGFP constructs only, the ratio between the Qdot and EGFP channels as a measure of membrane versus total receptor pool; iii) for all p75^{NTR} constructs, the intensities in Qdot channel as a measure of membrane abundance at the different levels of expression examined.

Cleaved Caspase-3 assay

Cortical neurons from wild type and p75^{NTR} KO mice were seeded on glass slides in 24-well dishes at medium-high density. On DIV1, KO neurons were transduced with S6- wt/mut p75^{NTR} lentiviral particles. On DIV2, transgene expression was induced with 0.05 μ g/ml doxycycline. On DIV3, neurons were treated for 12 h with 20 ng/ml human proBDNF or standard culture medium. Samples were then fixed in cold 1:1 acetone:methanol solution for 15 min at -20°C, washed three times in PBS, permeabilized with 0.5% Triton X-100 plus 2.5 % BSA/PBS 5 min at room temperature, blocked 1 h at room temperature with 5% BSA/PBS, incubated 2.30 h at room temperature with anti- cleaved caspase-3 (1:300, 9664 Cell Signaling Technology®) and anti- MAP-2 (1:2500, M9942 Sigma-Aldrich) antibodies in 2.5% BSA/PBS and stained 1 h at room temperature with relative fluorophore-conjugated secondary antibodies (anti rabbit-Alexa647, 1:100; anti mouse-Alexa488, 1:100, ThermoFisher). Glass slides were then mounted on glass coverslips with Fluoroshield™ (containing DAPI) and imaged at the confocal SP5 with HC PL FLUOTAR 20.0X air-objective (NA 0.5) and pinhole at 1.5 Airy Units. We used a 633 nm laser line and [648-718] nm emission window for Alexa647, a 488 nm laser and [500-600] nm emission window for Alexa488 and a pulsed 405 nm laser line with [410-500] nm emission range for DAPI. Cleaved caspase-3 positive neurons were defined as MAP2 positive cells displaying a mean intensity above an intensity threshold in the Alexa647 channel set according to evidently non-apoptotic cells in the untreated sample; neurons were counted in at least 6 fields per coverslip. All reagents were purchased from Sigma-Aldrich except where otherwise stated.

Detection of S6-tagged wt and mut p75^{NTR} from cell lysates by western blot

For blots shown in Figs. S1, S2 and S4, SH-SY5Y, PC12 or SK-N-BE(2) cells were transfected or transduced with S6-tagged wt or mut p75^{NTR} and induced with the indicated doxycycline (if not indicated, 1 μ g/ml doxycycline was used). After 24-48h induction, cells were lysed in RIPA buffer (Sigma-Aldrich®) supplemented with proteases inhibitors tablet

(Roche) and 1mM Phenylmethanesulfonyl fluoride (PMSF, Sigma-Aldrich®) for 15 min on ice. Lysates were centrifuged at 16,000 xg for 15 min at 4°C and quantified with Bradford assay. 20–35µg of each sample was mixed with SDS gel loading buffer and loaded on a standard 4–12% polyacrylamide Criterion™ XT Bis-Tris Protein Gel (Bio-Rad). The run was performed in MOPS 1x buffer (Bio-Rad) and transferred in Towbin 1x on a Nitrocellulose membrane (GE Healthcare). Membrane was blocked with Tris-buffered Saline, supplemented with 0.05% Tween-20® (TBST) and 5% Non-Fat Dry Milk (Bio-Rad), for 1h at room temperature and blotted with anti-p75^{NTR} (07-476 Millipore) 1:1000 diluted in TBST+ 5% Milk for 2h at room temperature. After three washes with TBST only, membrane was then blotted with Goat anti-Rabbit IgG (H+L)-HRP Conjugate (Bio-Rad) 1:2500 diluted in TBST + 5% Milk for 1h at room temperature. Membrane was washed and then imaged with ECL™ Western Blotting Detection Reagents (GE Healthcare). For blots shown in Fig. S14, SH-SY5Y cells were infected with S6-tagged wt or mut p75^{NTR} and induced for 24h with 1µg/ml doxycycline. Cells were lysed with TBS pH 7.4 supplemented with proteases inhibitors, 10mM Iodoacetamide, 60mM Octyl-β-D-glucopyranoside and 1% Triton X-100 (all reagents were purchased from Sigma-Aldrich®) for 15min on ice; lysates were then centrifuged at 16000 xg for 15 min at 4°C and protein contents were quantified with Bradford assay. 40 µg of each total cell extract was diluted both in DTT-containing 2X gel loading buffer (250mM Tris HCl pH 6.8 with 25% glycerol, 5% SDS, 0.05% Bromophenol Blue and 250mM DTT) and in DTT-missing 2X gel loading buffer (250mM Tris HCl pH 6.8 with 25% glycerol, 5% SDS, 0.05% Bromophenol Blue). DTT samples were boiled at 95°C for 5min, non-DTT samples were maintained at room temperature for 20min; then they were loaded on a 4–20% polyacrylamide Mini-PROTEAN® TGX™ Precast Protein gel (Bio-Rad) and run in Tris-Glycine-SDS 1X buffer (Bio-Rad). Transfer, blot and detection were performed as stated above. From a comparison between Figs. S4c and S14, it is evident that the run of high molecular weight bands (putative oligomeric p75^{NTR} species) depends on experimental conditions. In Fig. S4 a clear unique band at about 150kDa is visible for wt but not mut p75^{NTR}, which would match the molecular weight of a dimer. In Fig. S14 however, where samples are prepared with a different lysis buffer and a different gradient is used in the gel, wt p75^{NTR} runs as a double 50-75kDa band, and we observed a smear at higher molecular weights with two bands more visible in a region spanning from 150kDa to 250kDa, which would match the molecular weight of dimers or trimers. This smear was almost not visible for mut p75^{NTR}. However, in all conditions used in our studies, the band of the monomer was the predominant for either p75^{NTR} construct, similarly to what obtained by other groups using the 07-476 Millipore anti-p75^{NTR} antibody (18). We conclude that too many factors can affect the run of a protein in a gel, such as the antibody employed for detection, the lysis buffer, the length of a gel, the percentage of acrylamide or the use of denaturing or non-denaturing conditions. For these reasons, we preferred a direct and quantitative method for estimation of stoichiometry in a membrane of a cell, instead of using cell extracts.

Ex-vivo branching analysis in wt versus p75^{NTR} mice

Ex vivo analysis was performed on p75^{NTR} KO (5) and wt C57 female mice; animals were 5-6 months of age at the time of the experiment. All procedures were approved by the Italian Ministry of Health and are in compliance with the National Council of Research (CNR) guidelines. p75^{NTR} KO or C57 mice were anesthetized with avertin and injected bilaterally with 10⁹ vg AAV9.EF1a.DIO.eYFP.WPRE.hGH (Addgene 27056) and 10⁷ vg AAV1.hSyn.Cre.WPRE-hGH (Addgene 105553) in hippocampus CA3 (stereotaxic coordinates -1.9 AP, ±2.35 ML, -2.35 DV). AAV solution was adjusted with sterile PBS and 500nl were injected at 200nl/min in each hemisphere. After two weeks animals were anesthetized with avertin and perfused transcardially with 2% formaldehyde in PBS; after 5 hours in post-fixation, brains were cryoprotected in 30% sucrose PBS. 50µm slices were cut and mounted in Fluoroshield with DAPI (Sigma), and imaged with a Zeiss Axioskop microscope using a 40X air objective. Single axons emerging from CA3 area were identified and traced with NeuroLucida software (MBF Biosciences). The number of branch points was counted and normalized on the total length on the analysed axon. For NF-200 area calculation, 50µm slices were cut and processed for IF as follows: (i) blocked in PBST (PBS 0.3% Triton X-100) 10%FBS for 90', (ii) incubated overnight at 4°C with 10% FBS PBS anti-NF200 (abcam ab7795) 1:200, (iii) after 3 washes in PBS, incubated in 10%FBS PBS 0.1% Triton X-100 anti-mouse Alexa633 1:100 (Life Technologies) for 3 hours, (iv) incubated with 10µg/ml DAPI in PBS 0.1% Triton X-100 10', (v) washed three times in PBS and (vi) mounted with Vectashield (Vector Labs). A stack of 1024x1024 images (z-step 0.5µm) was acquired in the stratum radiatum of CA1 with confocal Leica SP5. After background subtraction, the maximum projection was taken and the resulting image was thresholded to remove pixels whose intensity was twice the mean intensity of the resulting background (calculated in an area devoid of axons). The threshold was kept constant for all samples, and the ratio of the supra-threshold area to the total area was quantified. For SYN1 points calculation, p75^{NTR} KO or C57 slices were taken and processed for immunofluorescence as above, with anti-SYN1 1:100 (Synaptic Systems 101011 clone 7.2) and anti-NMDAR2 1:100 (Synaptic Systems 244003), and secondary antibodies anti-mouse Alexa633 1:100, anti-rabbit Alexa555 1:100 (Life Technologies). 1024x1024 images from the stratum radiatum in CA1 were acquired with confocal SP5. After background subtraction, images were thresholded and particles were detected with ImageJ Analyze Particles feature. Only 0.5-5 µm² particles were considered, with 0.3-1 circularity. Before particle detection, Watershed feature was run to separate overlapping synapses. Areas of the images devoid of SYN1 puncta due to the presence of blood vessels were excluded from the analysis. The resulting calculated puncta number accounts for that, as it is normalized for the considered area.

Statistics

Statistical analysis was performed with OriginPro v9.0 or GraphPad Prism 6. Parametric tests used were Student's t-test (two-tailed), or one-way ANOVA with Bonferroni or Tukey's correction for multiple comparisons of more than two groups. Significance was set at $\alpha=0.05$. Comparisons between groups whose distributions were not normal, or requirements for parametric tests were not met, were performed with Kruskal–Wallis test, followed by Dunn's test for pairwise comparison. Nonparametric comparisons between two samples were performed with Mann–Whitey test. All information is summarized in Supplementary Table 3.

Readers will be able to access data, associated protocols, codes, and materials by directly contacting the corresponding authors.

Supplemental Figures

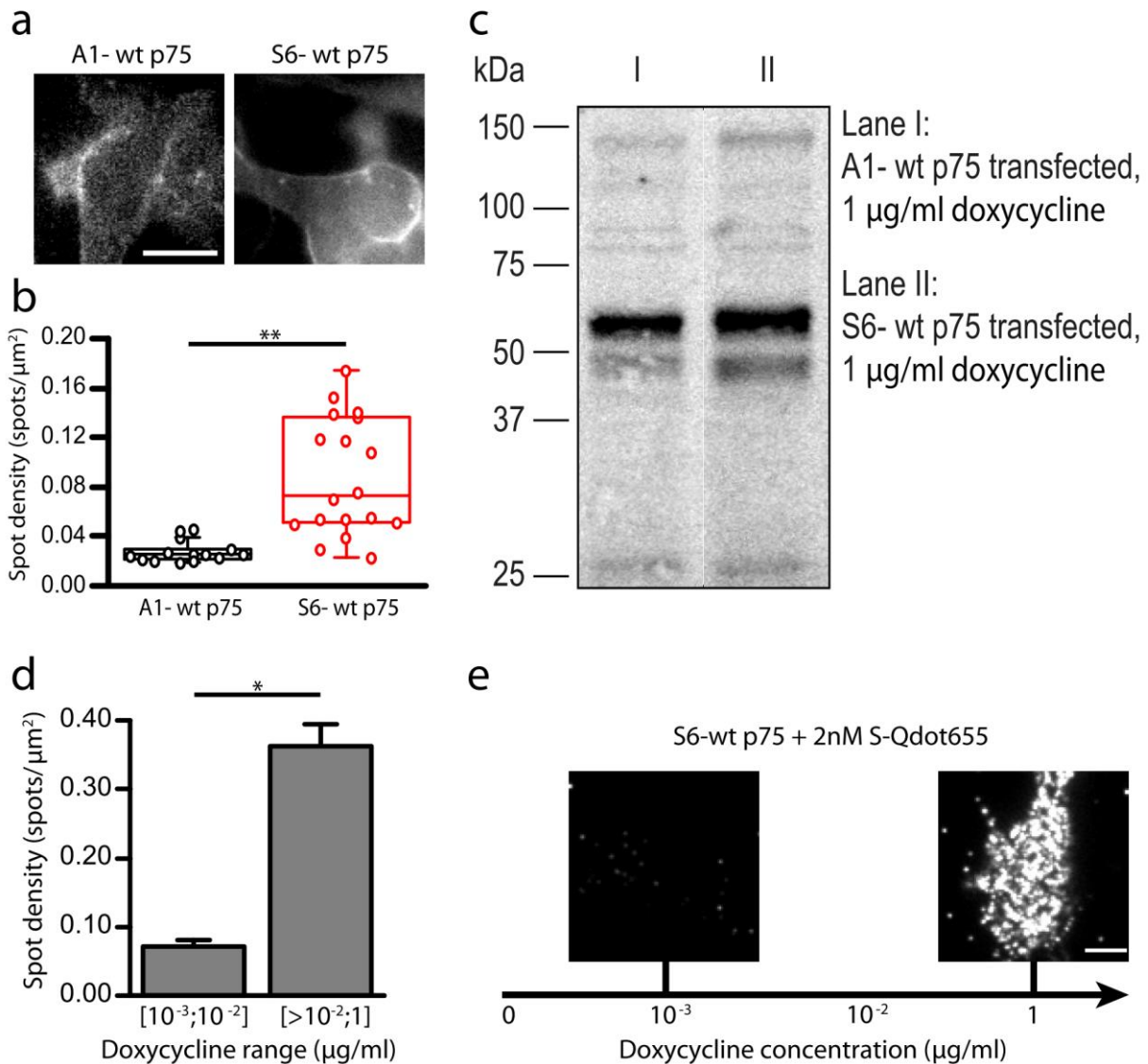


Fig. S1 S6-p75^{NTR} is labeled more efficiently than A1-p75^{NTR} (related to Fig. 1). (a) Typical SH-SY5Y cells expressing A1- or S6-tagged wt p75^{NTR} after receptor labeling. Cells were infected with lentivirus driving the expression of either of the two constructs under the tetracycline promoter and treated with 1 μg/ml doxycycline to induce expression. A1- or S6-tagged wt p75^{NTR} was labeled with 500nM Alexa488-CoA and Acp or Sfp synthase enzymes, respectively (1). Images were acquired at the TIRF microscope in epifluorescence mode. Scale bar, 10 μm. (b) At matching doses of doxycycline, labeled A1-p75^{NTR} is less abundant than S6-P75^{NTR}, as indicated by the lower number of spots per area in SH-SY5Y cells induced with 10⁻³ μg/ml doxycycline and labelled with 2nM streptavidin coated Qdot655 after receptor biotinylation (see Supplemental text for details about labeling). **P<0.01, Mann-Whitney test. Box plots are 25% - 75% range of the data, with median line. (c) Total cell lysates from SH-SY5Y cells expressing A1- or S6-wtP75 induced with 1 μg/ml doxycycline show slightly lower expression of the former, as seen in the anti-p75^{NTR} blot. Thus, lower A1-tag labeling is most probably due to a combination of lower expression and less efficient enzymatic reaction. (d-e) Considerations about S6 tag labeling efficiency. SH-SY5Y were infected with S6-tagged wt p75^{NTR} lentiviral particles, induced with 0, 10⁻³, 10⁻² or 1 μg/ml doxycycline, biotinylated and labelled with 2nM Qdot655. The density of spots per membrane area was quantified for cells in the different doxycycline ranges. The results, reported in panel d, demonstrate that the use of fluorescent probes in the nM range are not a limiting amount for exhaustive labeling of receptor in the low doxycycline concentrations (left), because the same Qdot concentration allows to obtain a much higher number of receptors labeled at high doxycycline doses (right). These data are consistent with previous reports demonstrating an efficiency of tag labeling close to 100% for chemical tags of the ACP family (19, 20). *P<0.013, Unpaired Student's t-test. Data are plotted as mean±S.E.M. Two representative TIRF images used in this quantification are reported in panel e. Scale bar, 5 μm.

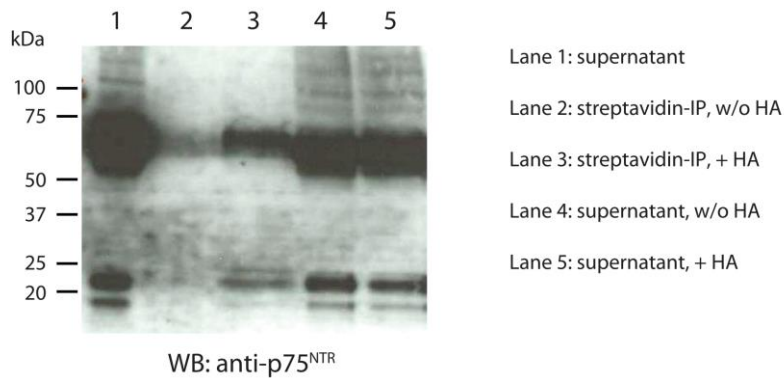


Fig. S2 Endogenous p75^{NTR} is palmitoylated in PC12 cells (related to Fig. 1). The Acyl-Biotinyl Exchange assay (see Supplemental methods for details) was performed on PC12 cells showing palmitoylation of endogenous p75^{NTR}. The total cell lysate (lane 1) is processed as described in Supplemental text, and pulled down with streptavidin beads (lane 3), while the supernatant is presented in lane 5. Removing hydroxylamine (HA) from the protocol impairs palmitic acid-biotin exchange: as a consequence, p75^{NTR} is not pulled down with streptavidin beads (lane 2), and is contained in the supernatant (lane 4). The panel shows the resulting anti-p75^{NTR} Western blot.

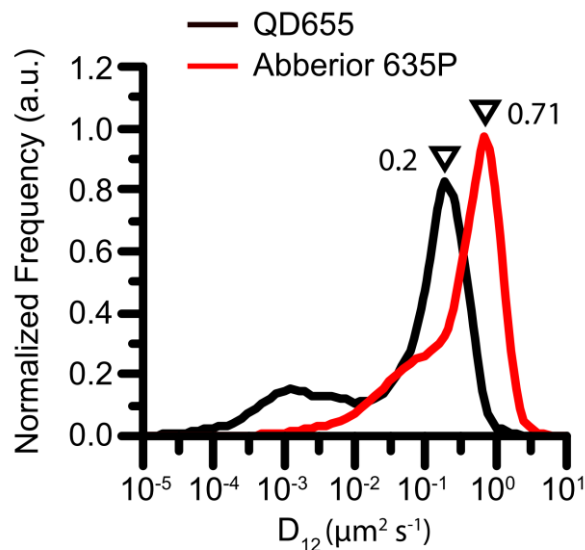


Fig. S3 p75^{NTR} diffusion coefficient distribution depends on the fluorescent label (related to Fig. 2). SH-SY5Y cells were transduced with S6-tagged wt p75^{NTR} viral particles and expression induced with 0.001-0.05 μg/ml doxycycline. Surface receptor molecules were either biotinylated and further labeled with 2nM streptavidin-coated Qdot655, or directly labeled with 25nM Abberior635P. After analysis of the trajectories in the two cases, we found that wt p75^{NTR} diffusion is influenced by the fluorophore size. Indeed, Qdot labeling after receptor biotinylation (black trace) determines a radically slower profile of the diffusion coefficient compared to the same receptor labeled with the smaller organic dye (red trace). Distribution peaks are indicated with arrowheads. Therefore, we always measured diffusion of p75^{NTR} fluorolabeled with small organic dyes.

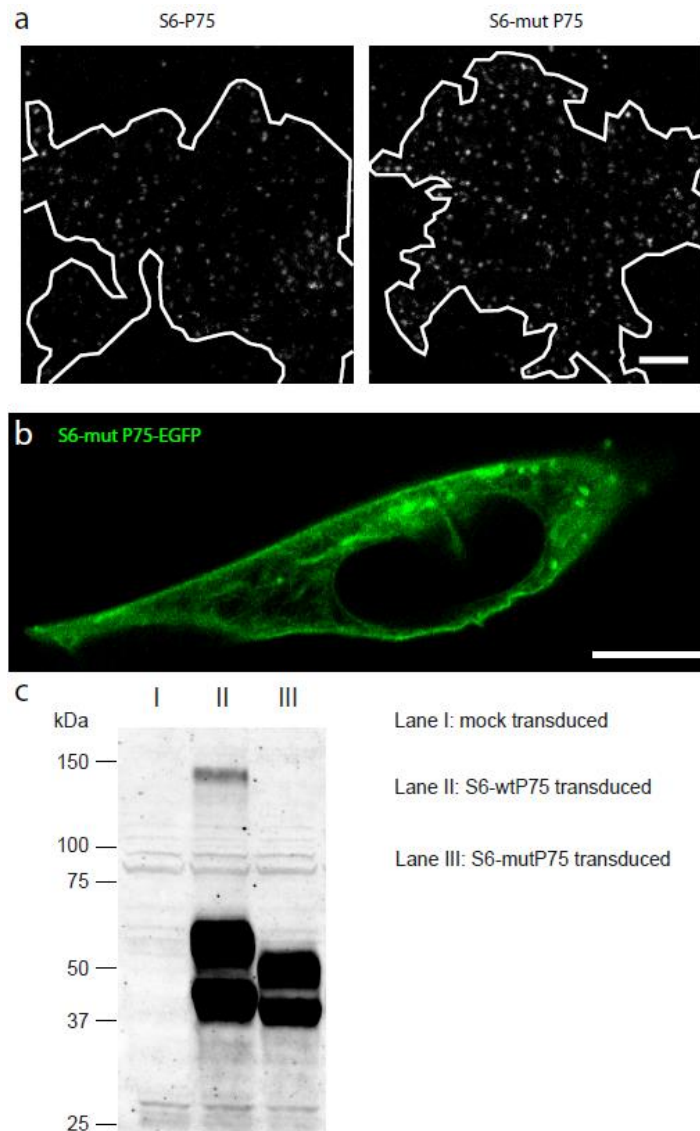


Fig. S4 S6-tagged mut p75^{NTR} localization is similar to the one of its cognate wt construct (related to Fig. 2). (a) S6-tagged mut p75^{NTR} is expressed and translocates to the surface of SK-N-BE(2) cells similarly to the wt counterpart. Cells were infected with lentiviral vector driving the doxycycline-dependent expression of the constructs, and visualized by TIRF microscopy after expression was induced with 0.05 μg/ml doxycycline. p75^{NTR} constructs were labelled with 5nM Abberior635P. Cell profiles are drawn with thick white lines. Scale bar, 5 μm. (b) EGFP-fused S6-tagged mut p75^{NTR} localizes both to the plasma membrane and to the nuclear envelope, as S6-tagged wt p75^{NTR}. Confocal image of SH-SY5Y cells transfected with S6-tagged mut p75^{NTR}-EGFP. Scale bar, 5 μm. (c) anti-p75^{NTR} Western Blot from transfected SK-N-BE(2) confirms S6-tagged mut p75^{NTR} expression and integrity compared to the cognate wt construct. S6-tagged mut p75^{NTR} has a slightly lower molecular weight than S6-tagged wt p75^{NTR} due to the deletion of the juxtamembrane region (see Fig. 2c and relative methods). Note the complete absence of the higher molecular weight band in the mut construct lane, that is instead present in the wt p75^{NTR} lane, although representing a small fraction of the whole p75^{NTR} population.

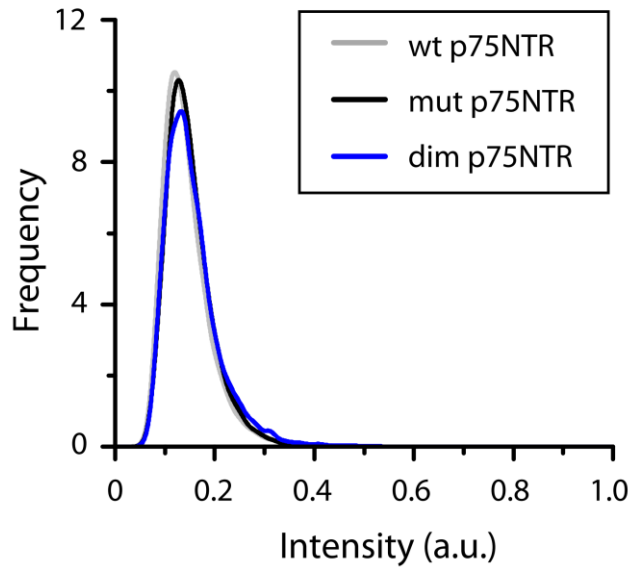


Fig. S5 Average intensities of wt, mut and dim p75^{NTR} trajectories (related to Fig. 3). Trajectories retrieved from SK-N-BE(2) cells expressing wt, mut and dim p75^{NTR}, whose *D*, *M&S*, and *Td* quantification are reported in Fig. 2, were also analyzed for their average intensities. The I_{av} distributions, obtained as in (14), show no substantial differences among the three constructs, although a slightly higher high- I_{av} tail could be noticed for dim p75^{NTR}.

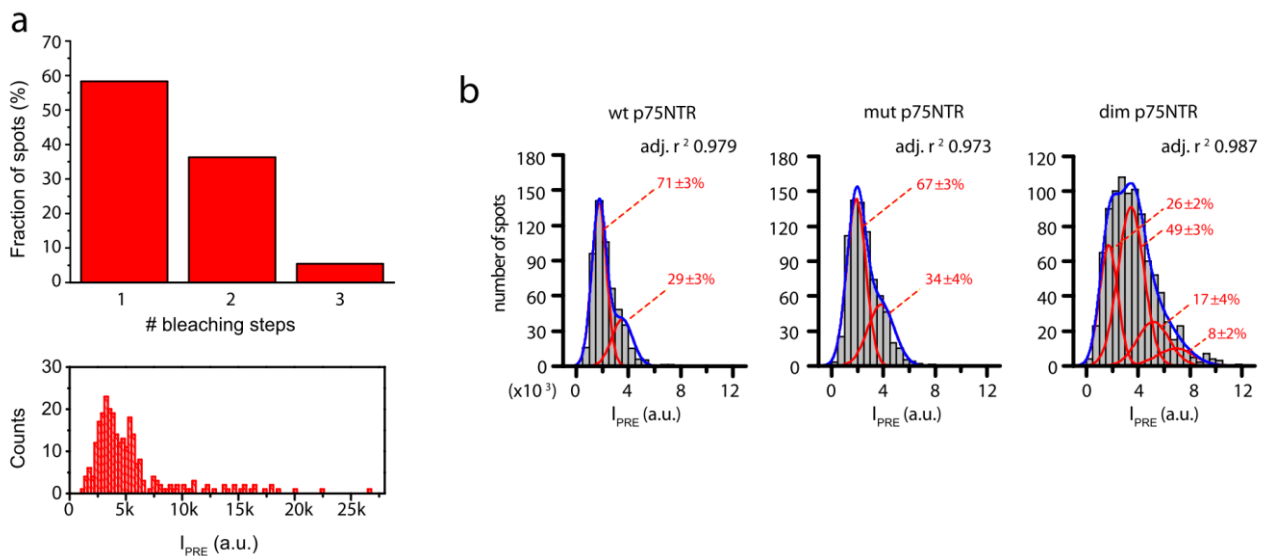


Fig. S6 Single step photobleaching analysis for TrkA and p75^{NTR} constructs (related to Fig. 3). (a) Single step photobleaching analysis for SK-N-BE(2) cells expressing S6-tagged TrkA construct (1) after 15 minutes of NGF treatment readily identifies monomers and dimers. More than 40% of the step-photobleached spots has two (or more) photobleach steps (top panel), and two peaks are clearly visible in the I_{PRE} distribution, corresponding to the monomeric and dimeric species (bottom panel). Note the non-negligible presence of species with pre-bleach intensity higher than 7500 a.u., that can be identified in the I_{PRE} histogram and most likely correspond to oligomeric forms of activated receptors whose intensity profiles do not completely bleach in the observation time and for this reason are excluded from the photobleaching steps count (see Methods for details of quantification). (b) I_{PRE} distributions (gray-column histograms) obtained for the three p75^{NTR} constructs analyzed in Fig. 3 with multigaussian fits superimposed (thick blue curve; thin red curves are the single fitted gaussians).

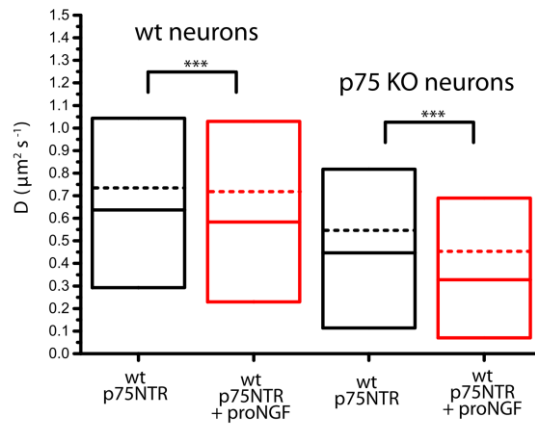


Fig. S7 Diffusivity of wt p75^{NTR} receptor particles in the absence or presence of proNGF in cortical neurons (related to Fig. 4). Cortical neurons from wt and p75^{NTR} KO neonatal mice were cultured and transduced with wt p75^{NTR} lentiviral particles; transgene expression was induced with 0.05 $\mu\text{g}/\mu\text{l}$ doxycycline and receptor molecules labeled with Abberior 635P dye. Box-plot for D values retrieved from trajectories collected from DIV3 wt (left) and p75^{NTR} KO (right) neurons in resting conditions (black) and up to 15 min after proNGF administration (red) are reported. Cells displaying a density of membrane receptors in the [0.1-0.4] spots/ μm^2 range were considered for this analysis (average spot density wt neurons: 0.36 ± 0.05 (unst); 0.35 ± 0.04 (proNGF); p75 KO neurons: 0.22 ± 0.08 (unst); 0.24 ± 0.06 (proNGF)). Boxes: 25th-75th percentiles; line: median; dashed line: mean. ***P<0.001 Kruskal-Wallis test, with Dunn's means comparison.

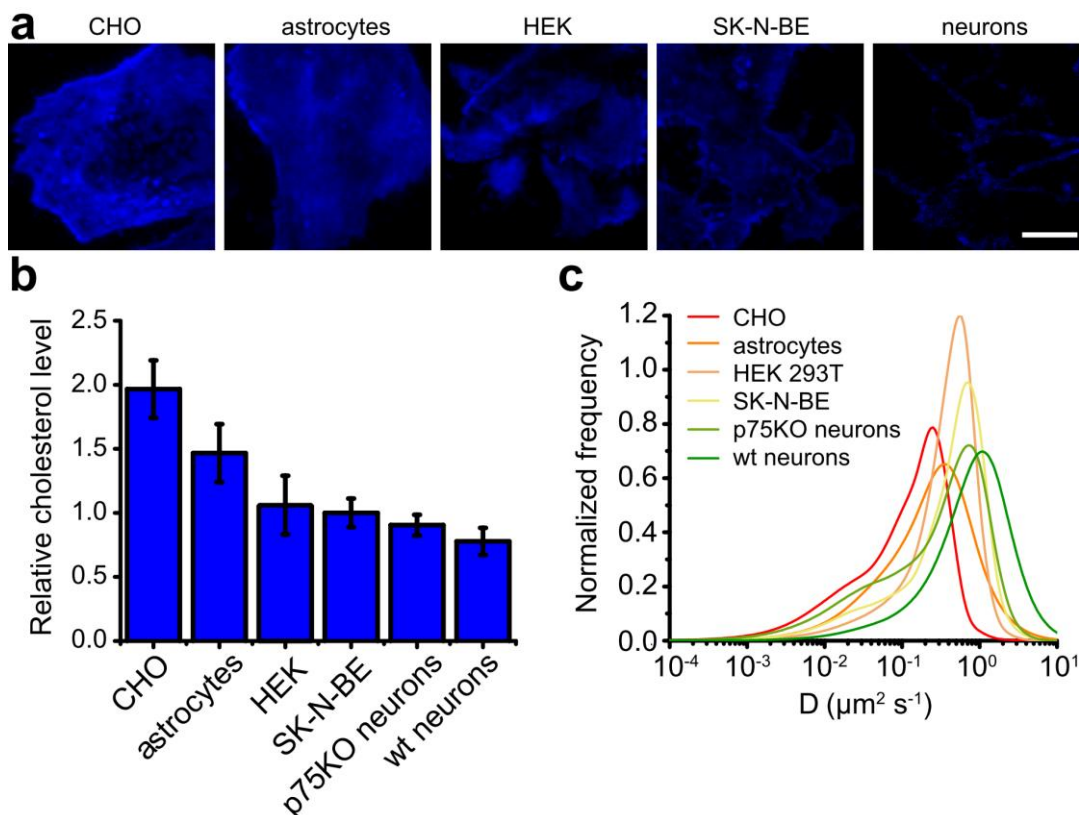


Fig. S8 p75^{NTR} diffusion coefficient depends on cholesterol cell content (related to Fig. 4). (a) Representative TIRF images of membrane filipin III staining for different cell models. Scale bar, 10 μm . (b) Quantification of the cholesterol content for the various cell models. Values are normalized on the SK-N-BE(2) value. Bars are mean \pm S.D. (c) Characteristic D distribution of S6-tagged wt p75^{NTR} in different cellular models. The D distribution in the various cell

types follows the relative cholesterol level order, with cells containing higher cholesterol levels displaying lower D values and vice-versa.

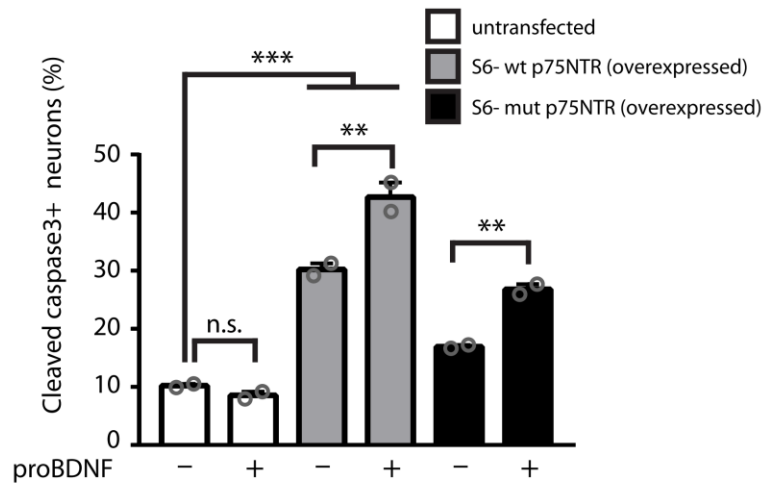


Fig. S9 When overexpressed, both wt and mut p75^{NTR} are able to induce apoptosis (related to Fig. 5). Percentage of cleaved caspase-3 positive cortical neurons from p75^{NTR} KO mice, transduced with S6-tagged wt or mut p75^{NTR} lentiviral particles. Transgene overexpression was induced with 1 μ g/ml doxycycline, and cultures treated with proBDNF for 12 hours as outlined in Fig. 5a. Overexpressing wt p75^{NTR} significantly increases the proportion of apoptotic neurons, and overexpressing mut p75^{NTR} rescues its ability to induce apoptosis upon proBDNF administration. Along with results in Fig. 5, our interpretation is that, under overexpression conditions, the occupancy of cholesterol-rich areas (where apoptotic signaling can start) is also increased as a consequence of total membrane pool increase. This would explain the ability of mut p75^{NTR} to induce apoptosis under proBDNF stimulus, and would also explain the higher number of apoptotic cells in cultures expressing wt p75^{NTR} even in the absence of proBDNF. Bars represent mean \pm sem, n.s. is not significant at the 0.05 level, ***P<0.001, **P<0.01 one-way ANOVA with Tukey's comparison of means.

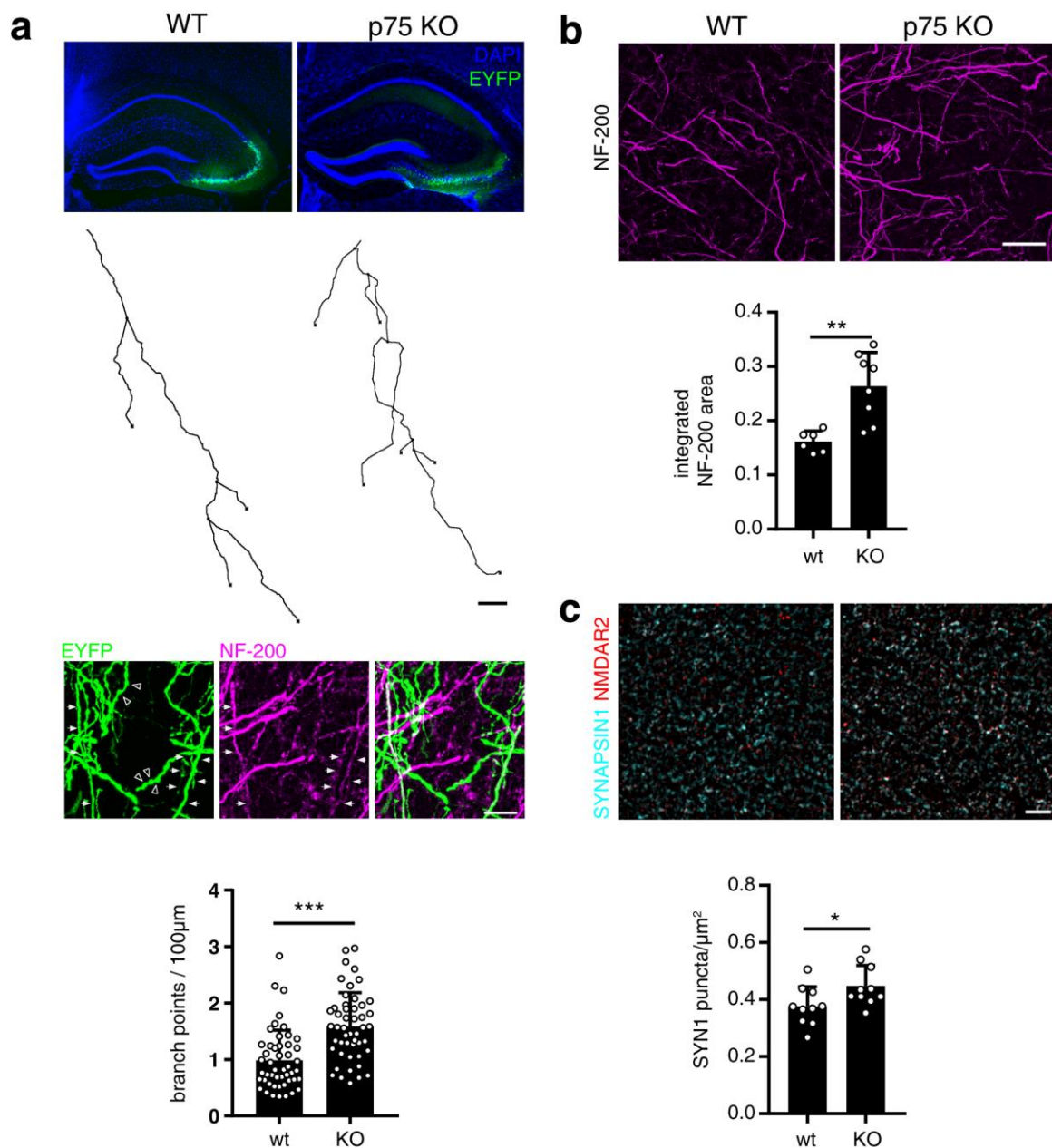


Fig. S10 p75^{NTR} KO mice display increased axon complexity than wt ones (related to Fig. 6). (a) wt and p75 KO animals were injected with an AAV encoding floxed EYFP and limiting hSYN:Cre AAV in the CA3 area, driving the sparse expression of EYFP (green) in CA3 neurons; nuclei were stained with DAPI (blue). Axons in the CA1 area were traced with NeuroLucida softwares (black profiles below), showing a higher number of branching points per unit of length for the p75 KO mice; scale bar, 10µm. Below, we confirmed that the traced EYFP-positive neurite are axons as they are either strongly immunoreactive to axonal marker NF200 (arrowheads) or are terminal axonal tracts displaying varicosities (empty arrowheads); scale bar 10µm. On the bottom, quantification of axonal branch points per length, ***P<0.001 Mann-Whitney test. (b) Consistently, the area occupied by NF200⁺ axons (magenta) is larger in p75^{NTR} KO than wt mice in CA1 stratum radiatum; scale bar, 20µm. Below, quantification of the fraction of area occupied by axons; **P<0.01 Mann-Whitney test. (c) This is also reflected in the higher synapse density observed in p75^{NTR} KO mice in the CA1 stratum radiatum, evaluated as a higher density of SYN1 positive puncta. We confirmed that the identified SYN1 puncta (cyan) are juxtaposed to postsynaptic marker NMDAR2 (red). Scale bar, 5µm. Below, quantification of SYN1 puncta per area. *P<0.05 Mann-Whitney test. Bars are mean±sd.

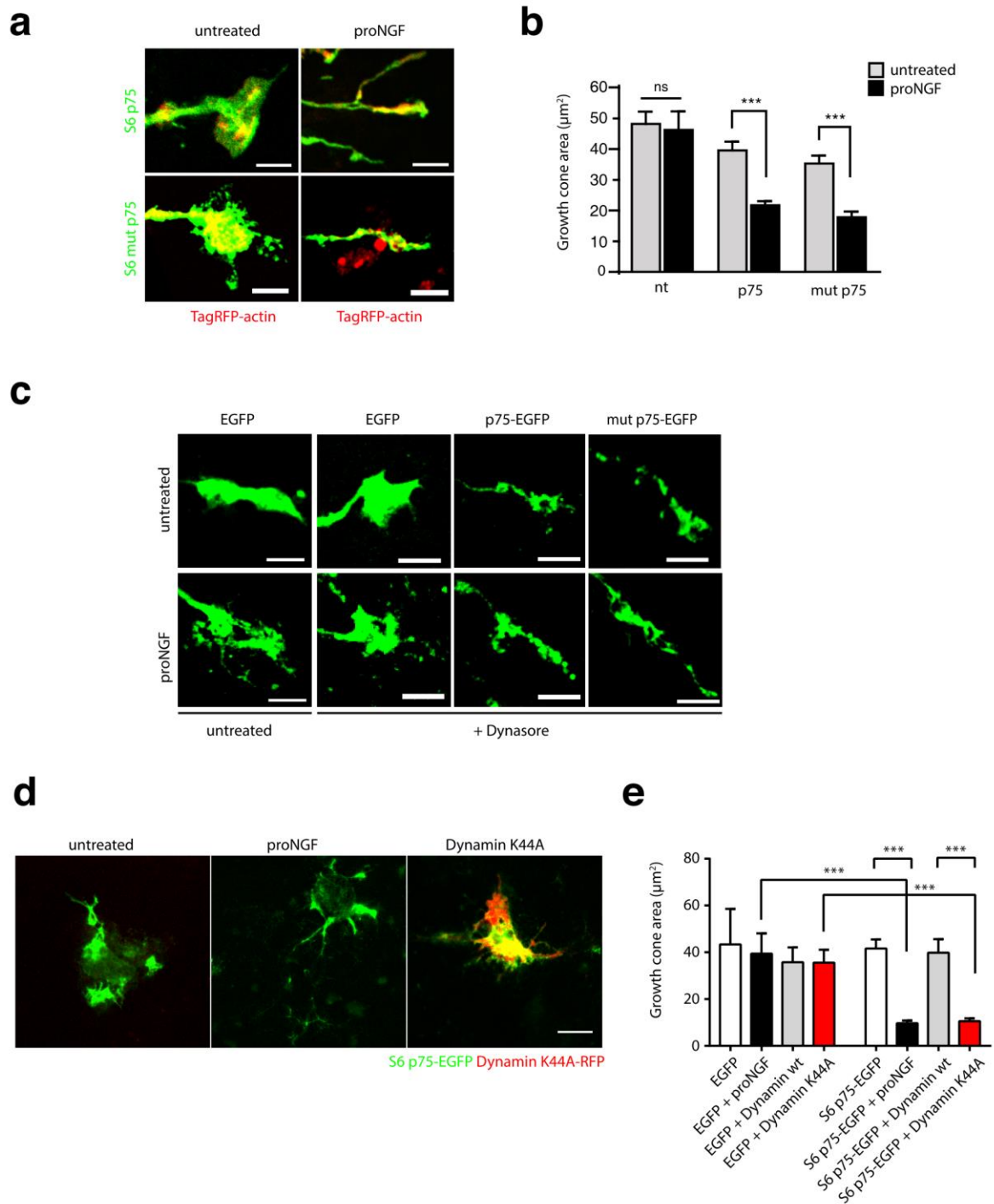


Fig. S11 Surface p75^{NTR} causes growth cone collapse (related to Fig. 7). (a) Representative confocal images of growth cones of wt hippocampal neurons, transfected with S6-tagged wt and mut p75^{NTR}-EGFP constructs, untreated or incubated with proNGF for 30'. Scale bar, 5 μm . The corresponding growth cone area is quantified in (b), in comparison to a non-transfected control (nt). *** $P < 0.001$, ns: not significant at the 0.05 level in a one-way ANOVA, Bonferroni multiple comparisons. Bars are means \pm sem. (c) Representative images of growth cones for wt and mut p75^{NTR}-EGFP (or EGFP only) transfected in wt hippocampal neurons, untreated or treated with Dynasore in the absence or presence of proNGF, as indicated. Quantification is reported in Fig. 7f. (d) Inhibition of p75^{NTR}-EGFP internalization with co-expression of dominant negative (DN) K44A Dynamin-RFP is sufficient to induce growth cone collapse in the absence of proNGF. Scale bar, 10 μm . (e) Quantification of growth cone area for EGFP- or wt S6-p75^{NTR}-EGFP- expressing neurons. DN, but not wt, Dynamin co-expression, caused growth cone collapse. *** $P < 0.001$ one-way ANOVA, Tukey's comparison of means.

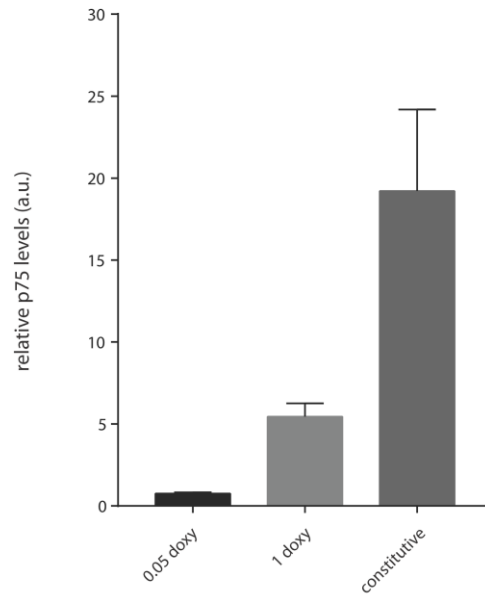


Fig. S12 p75^{NTR} expression levels in the various conditions tested in our study (related to Figs. 6-7). p75^{NTR} levels were measured quantifying the intensity of QDot-labeled p75^{NTR} in wt neurons. Neurons were infected with TRE-S6 p75^{NTR} lentivirus and induced with 0.05 or 1 μ g/ml doxycycline, or transfected with CMV-S6 p75^{NTR}-EGFP (constitutive). Bars are mean \pm s.e.m.

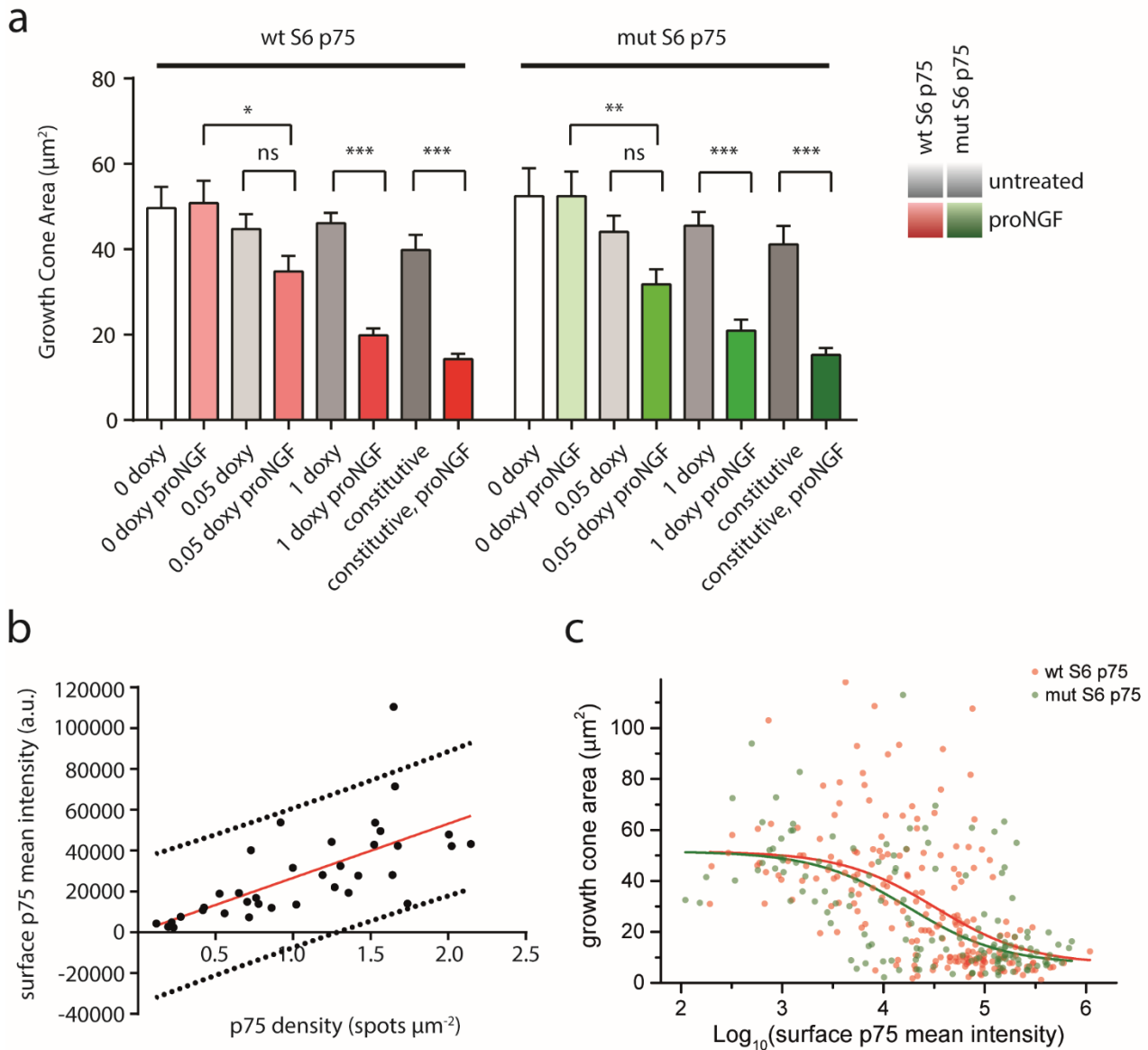


Fig. S13 p75^{NTR} causes growth cone collapse in a concentration-dependent manner (related to Figs. 6-7). (a) Quantification of growth cone area for wt (left) or mut (right) p75^{NTR} at various expression levels as in Fig. S12. Infected neurons were induced with 0, 0.05 or 1 $\mu\text{g/ml}$ doxycycline, or transfected with CMV-S6 (wt/mut) p75^{NTR}-EGFP (constitutive), and left untreated or treated with proNGF for 30 minutes. * $P < 0.05$ ** $P < 0.01$ *** $P < 0.001$ one-way ANOVA, Tukey's comparison of means. (b) p75^{NTR} molecules were biotinylated before proNGF treatment, then the surface pool was labeled with Streptavidin-QDot655 (see Fig. 7). The mean intensity of the QDot channel is a good estimate of the density of receptors per μm^2 . Regression line is in red, with $\pm 95\%$ prediction bands (dotted black lines; $r^2 = 0.5821$, ANOVA on regression $F = 39$, $df(1,28)$ $P < 0.0001$). (c) Dependency of growth cone area on the surface intensity of wt (red dots) or mut (green dots) shows a similar sigmoidal trend. Data from the samples induced at 0, 0.05 and 1 $\mu\text{g/ml}$ doxycyclin and treated with proNGF are included for both receptors. The populations of growth cone areas for the two receptors are not significantly different from each other (Kolmogorov-Smirnov test, $P = 0.1349$). Red and green curves are guide for the eyes for the behavior of data from wt p75^{NTR} and mut p75^{NTR}, respectively (curves are sigmoid fits with extremes and slope obtained from the pooled data).

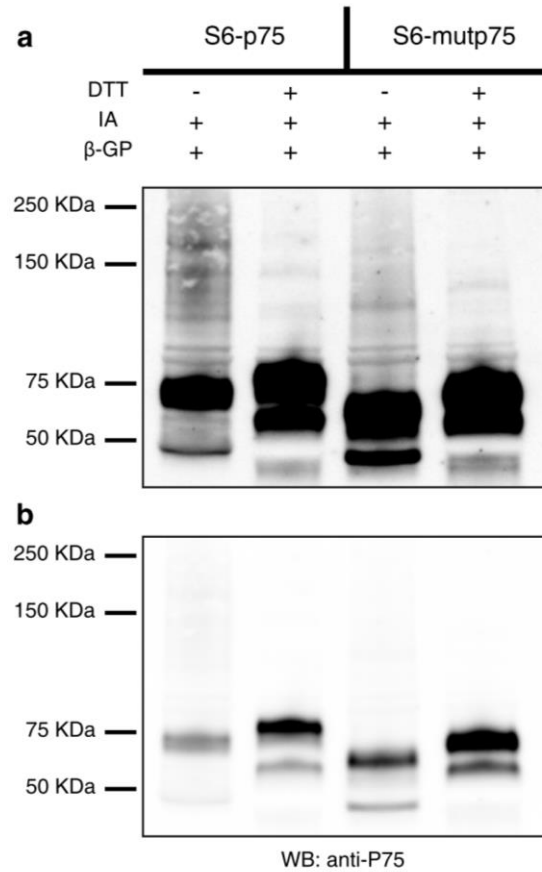


Fig. S14 Putative oligomeric p75^{NTR} species detected in western blot experiments. S6-tagged wt p75^{NTR} and mut p75^{NTR} were infected in SH-SY5Y cells and induced with 1 μ g/ml doxycycline. Lysis was performed as reported in (21): Octyl- β -D-glucopyranoside (β -GP) and iodoacetamide (IA) were added to lysis solution. Equal amounts of total cell lysates (40 μ g) were supplemented with a 2X loading buffer with or without dithiothreitol (DTT) and loaded on a 4-20% acrylamide gradient gel. The anti-p75^{NTR} Western blot shows the presence of a higher molecular-weight smear, including the bands corresponding to putative dimeric (150 kDa) and trimeric (circa 215 kDa) oligomeric species of wt p75^{NTR}, which are absent in the mut p75^{NTR} lanes. The blot reported in panel (a) was exposed to saturation to see the higher-molecular weights bands; the standard-exposed blot is presented in panel (b).

Supplemental Videos

Video S1 Typical 500-frame TIRF movie of a living SK-N-BE(2) cell expressing S6-tagged p75^{NTR} and labeled with CoA-Abberior635P (~0.39 spots/ μm^2) moving in plasma membrane. Scale bar, 5 μm .

Video S2 Typical 500-frame TIRF movie of a living, DIV3 cortical p75^{NTR} KO neuron expressing S6-tagged p75^{NTR} and labeled with CoA-Abberior635P (~0.38 spots/ μm^2). A mask, drawn on movie maximum intensity projection, was applied to exclude surrounding astrocytes signals, and fluorophores adhered to the glass because of PDL coating. Scale bar, 5 μm .

Video S3 Output of single particles detection and tracking by u-track software on a SK-N-BE(2) cell expressing S6-tagged p75^{NTR} and labeled with CoA-Abberior635P (~0.27 spots/ μm^2). Trajectories are reported in blue.

Video S4 Representation of a merge (S4) event in a SH-SY5Y cell surface expressing CoA-Abberior635P-labeled S6-tagged p75^{NTR}. Continuous blue lines are single particles tracks over time, blue triangles pointing upwards represent the beginning of a track, blue triangles pointing rightwards and red line show two distinct particles merging in a single one (SV4), asterisks depict gaps in particle tracking. Scale bars, 1 μm .

Video S5 Representation of a split (S5) event in a SH-SY5Y cell surface expressing CoA-Abberior635P-labeled S6-tagged p75^{NTR}. Continuous blue lines are single particles tracks over time, blue triangles pointing upwards represent the beginning of a track, blue triangles pointing leftwards and green line indicate a split event of one particle in two distinct trajectories, asterisks depict gaps in particle tracking. Scale bars, 1 μm .

Supplemental References

1. Marchetti L, et al. (2014) Site-specific labeling of neurotrophins and their receptors via short and versatile peptide tags. *PLoS One* 9(11). doi:10.1371/journal.pone.0113708.
2. Gobbo F, Bonsignore F, Amodeo R, Cattaneo A, Marchetti L (2018) Site-specific direct labeling of neurotrophins and their receptors: From biochemistry to advanced imaging applications. *Methods in Molecular Biology*, pp 295–314.
3. Youker RT, et al. (2013) Multiple motifs regulate apical sorting of p75 via a mechanism that involves dimerization and higher-order oligomerization. *Mol Biol Cell*. doi:10.1091/mbc.E13-02-0078.
4. Hynes TR, Mervine SM, Yost EA, Sabo JL, Berlot CH (2004) Live cell imaging of Gs and the β 2-adrenergic receptor demonstrates that both α s and β 1 γ 7 internalize upon stimulation and exhibit similar trafficking patterns that differ from that of the β 2-adrenergic receptor. *J Biol Chem*. doi:10.1074/jbc.M405151200.
5. Taylor MJ, Perrais D, Merrifield CJ (2011) A high precision survey of the molecular dynamics of mammalian clathrin-mediated endocytosis. *PLoS Biol*. doi:10.1371/journal.pbio.1000604.
6. Storti B, Bizzarri R, Cardarelli F, Beltrami F (2012) Intact microtubules preserve transient receptor potential vanilloid 1 (TRPV1) functionality through receptor binding. *J Biol Chem*. doi:10.1074/jbc.M111.332296.
7. Lee KF, et al. (1992) Targeted mutation of the gene encoding the low affinity NGF receptor p75 leads to deficits in the peripheral sensory nervous system. *Cell*. doi:10.1016/0092-8674(92)90286-L.
8. Gobbo F, et al. (2017) Activity-dependent expression of Channelrhodopsin at neuronal synapses. *Nat Commun*. doi:10.1038/s41467-017-01699-7.
9. Capsoni S, et al. (2017) The chemokine CXCL12 mediates the anti-amyloidogenic action of painless human nerve growth factor. *Brain*. doi:10.1093/brain/aww271.
10. Wan J, Roth AF, Bailey AO, Davis NG (2007) Palmitoylated proteins: Purification and identification. *Nat Protoc*. doi:10.1038/nprot.2007.225.
11. De Nadai T, et al. (2016) Precursor and mature NGF live tracking: One versus many at a time in the axons. *Sci Rep* 6. doi:10.1038/srep20272.
12. Rattenholl A, et al. (2001) The pro-sequence facilitates folding of human nerve growth factor from Escherichia coli inclusion bodies. *Eur J Biochem*. doi:10.1046/j.1432-1327.2001.02232.x.
13. Paoletti F, et al. (2009) Intrinsic structural disorder of mouse proNGF. *Proteins Struct Funct Bioinforma*. doi:10.1002/prot.22311.
14. Marchetti L, et al. (2013) Ligand signature in the membrane dynamics of single TrkA receptor. *J Cell Sci* 126(19):4445–4456.
15. Jaqaman K, et al. (2011) Cytoskeletal control of CD36 diffusion promotes its receptor and signaling function. *Cell* 146(4):593–606.
16. Tanaka KAK, et al. (2010) Membrane molecules mobile even after chemical fixation. *Nat Methods*. doi:10.1038/nmeth.f.314.
17. Zhang W, et al. (2009) Single-molecule imaging reveals transforming growth factor- β -induced type II receptor dimerization. *Proc Natl Acad Sci U S A*. doi:0908279106 [pii]r10.1073/pnas.0908279106.
18. Sykes AM, et al. (2012) The effects of transmembrane sequence and dimerization on cleavage of the p75 neurotrophin receptor by γ -secretase. *J Biol Chem*. doi:10.1074/jbc.M112.382903.
19. Kasai RS, et al. (2011) Full characterization of GPCR monomer-dimer dynamic equilibrium by single molecule imaging. *J Cell Biol*. doi:10.1083/jcb.201009128.
20. Meyer BH, et al. (2006) FRET imaging reveals that functional neurokinin-1 receptors are monomeric and reside in membrane microdomains of live cells. *Proc Natl Acad Sci*. doi:10.1073/pnas.0507686103.
21. Anastasia A, Barker PA, Chao M V., Hempstead BL (2015) Detection of p75NTR Trimers: Implications for Receptor Stoichiometry and Activation. *J Neurosci*. doi:10.1523/JNEUROSCI.0591-15.2015.
22. Vilar M, et al. (2009) Activation of the p75 neurotrophin receptor through conformational rearrangement of

disulphide-linked receptor dimers. *Neuron* 62(1):72–83.

23. Vilar M, et al. (2009) Ligand-independent signaling by disulfide-crosslinked dimers of the p75 neurotrophin receptor. *J Cell Sci* 122(Pt 18):3351–7.
24. Yaar M, et al. (2002) Amyloid β binds trimers as well as monomers of the 75-kDa neurotrophin receptor and activates receptor signaling. *J Biol Chem*. doi:10.1074/jbc.M110929200.
25. Langevin C, Jaaro H, Bressanelli S, Fainzilber M, Tuffereau C (2002) Rabies virus glycoprotein (RVG) is a trimeric ligand for the N-terminal cysteine-rich domain of the mammalian p75 neurotrophin receptor. *J Biol Chem*. doi:10.1074/jbc.M201374200.
26. Nadezhdin KD, et al. (2016) Structural basis of p75 transmembrane domain dimerization. *J Biol Chem*. doi:10.1074/jbc.M116.723585.

Supplemental Tables

Table S1: List of technical details of main works reporting p75^{NTR} oligomerization detected as shifted protein band by western blot analysis. We report for each work: Reference, specie of p75^{NTR} sequence analyzed (**r**: rat sequence; **m**: mouse sequence; **h**: human sequence), cell type probed, lysis conditions (where not specified, traditional lysis conditions are used), type of gel used in the SDS-PAGE, antibody used for the WB detection, and abundance and molecular weight (MW) of the shifted p75^{NTR} band.

Reference	p75 ^{NTR} specie (r,m,h)	Cell type	Cell Lysis Conditions	Type of SDS-PAGE Gel	Detection	MW of the shifted band and relative abundance
(22)	Endogenous-r Construct-r	PC12 SCG RN22 Hippocampus Cortex Cerebellum HEK COS7	+ oGlucosyde + iodoacetamide	n.d.	WB anti-p75 ^{NTR} (MC192 antibody)	Clear dimer with variable abundance, mostly dimers in neurons or at high expression.
(23)	Construct-r	COS7	+ oGlucosyde + iodoacetamide	n.d.	WB anti-p75 ^{NTR} (MC192 antibody)	Dimer:Monomer 1:1
(21)	Construct-m Construct-h Endogenous-m Endogenous-r	HEK Cortex DRG PC12	+ oGlucopyranoside + iodoacetamide	Big (17x17 cm)	WB anti-p75 ^{NTR} (Covance #PRB- 602C or R&D Systems #AF367)	Mainly trimer up to 1:1 with monomer
(18)	Construct-r	HEK	Normal, with or without crosslinking	gradient	WB anti-p75 ^{NTR} (Millipore 07- 476) + anti-His tag	Faint Dimer band
(24)	Endogenous-r Construct-h	Cortex NIH3T3- p75 ^{NTR}	Normal after DTSSP crosslinking	n.d.	WB anti-p75 ^{NTR} (Anti-human and anti-rat antibodies from Roche Molecular Biochemicals)	Faint trimer band in cortex, trimer:monomer 1:1 in NIH3T3
(25)	Construct-h	SKNBE(2) COS	+ NEM	n.d.	WB anti-p75 ^{NTR} antibodies (monoclonal ME20.4, ATCC or polyclonal Promega)	trimer:monomer 1:1 with the monoclonal antibody; faint trimer band with the polyclonal antibody
(26)	Construct-h	HELA	+ iodoacetamide after BS3 crosslinking	n.d.	WB anti-p75 ^{NTR} antibody (polyclonal Promega)	Dimer band less represented than monomer

n.d. = not described

Table S2: List of cloning and mutagenesis primers.

Primer name and length	Primer sequence (5' → 3')
P75 ^{NTR} -insert1-FW (54mer)	gggggtgcccttgagggtgccggagattcttctaaggaggcatgccccacaggc
P75 ^{NTR} -insert1-RV (54mer)	gcctgtggggcatgcctccttaagagaatctccggcacctccaaggacacccc
P75 ^{NTR} -S ₆ insert2-FW (66mer)	ggagggtgccggagattctcttctgtggctgcttaggcttttgaataaggaggcatgccccacaggc
P75 ^{NTR} -S ₆ insert2-RV (66mer)	gcctgtggggcatgcctccttattcaaaagcctaagcagccacgaaagagaatctccggcacctcc
S ₆ P75 ^{NTR} -Nterm-FW (36mer)	cacgaggctagcacgcgtatgggggcagggtgccacc
S ₆ P75 ^{NTR} -CRD4-RV (46mer)	cgagcggatccaccgcctccacctccgccagggatctcctcgact
P75 ^{NTR} -LeuZip-FW (29mer)	cgagcggatccctggagagaatcgcccgg
P75 ^{NTR} -LeuZip-RV (36mer)	ctaggcggtagcactttctgtttaagctgtgccac
S ₆ P75 ^{NTR} -JM-FW (48mer)	ctaggcggtagcactttctgtttaagctgtgccac
S ₆ P75 ^{NTR} -Cterm-RV (38mer)	ccagtcctcgagacgcgttcacaccggggatgtggcag
P75 ^{NTR} -MluI-FW (32mer)	gtcagctgacgcgtatgggggcagggtgccacc
P75 ^{NTR} -MluI-RV (35mer)	cagtcgacacgcgttcacaccggggatgtggcagt

Table S3. Statistics information. The table lists the figure or panel number (**Figure**), the name (**Sample**) and the numerosity (**n**) of analysed samples, the number of independent measures (**Replicates : R**), a description of the sample (**Notes**) and the details of statistic test used for analysis (**Statistics**).

Figure	sample	n	R	Notes	Statistics
1d	wt p75 transduced neurons	19	1	n are neurons	Paired Student's t-test, two-tailed t=-10.9 dF= 18 P=2.32494E-9
1e	NT	37	2	n are growth cones	one-way ANOVA, Kruskal-Wallis test, followed by Dunn's comparison n=4,178 S=55.55 P<10E-5 NT vs NT +proNGF P>0.999 P75 vs P75 +proNGF P>10E-4
	NT +proNGF	20	2		
	P75	62	2		
	P75 +proNGF	66	2		
1f	wt	3	3	2064 neurons	unpaired Student's t.-test (two-tailed), Welch's correction for unequal variance t=10.3 dF=2.059 P=0.0084
	wt pro	3	3	1850 neurons	
	KO	3	3	4500 neurons	one-way ANOVA, followed by Tukey's comparisons dF=3,10 F=226.6 P<10E-5 KO vs KO pro P=0.7323 KO vs KO P75 P=0.8110 KO P75 vs KO P75 pro P<10E-4
	KO pro	3	3	5337 neurons	
	KO P75	4	4	4685 neurons	
	KO P75 pro	4	4	4601 neurons	
2d	wt p75	180491	4	trajs from 43 cells	NA
	mut p75	207280	4	trajs from 47 cells	
	dim p75	108422	5	trajs from 43 cells	
2e	wt P75	43	4	n are analyzed cells	one-way ANOVA, followed by Bonferroni's comparison dF=2,130 F=14.37 P<0.0001 wt p75 vs mut P75 n.s. wt P75 vs dim P75 P<0.0001 mut P75 vs dim P75 P<0.0001
	mut P75	47	4		
	dim P75	43	5		
2g	wt p75	3977	4	n are trajectories corresponding to Td events in the cells reported in Fig. 2e	NA
	mut p75	4106	4		
	dim p75	1803	5		
3c	P75	416	3	n are spots from 15 cells	Chi-square test $\chi^2 = 347.7$, df=6 P<0.0001
	mut P75	653	3		
	dim P75	816	3		
4a	dim p75	132251	5	trajs from 69 cells	Kruskal-Wallis test (P < 0.0001) followed by Dunn's comparison of means (P < 0.001 considered as significant)
	wt p75	59237	4	trajs from 34 cells	
	wt p75 + NGF	65387	4	trajs from 37 cells	
	mut p75	85615	4	trajs from 27 cells	
	mut p75 + NGF	103472	4	trajs from 38 cells	
4b (cholesterol)	CHO	90	8	n are analyzed fields	Linear fit adj r ² =0.97612, ANOVA of regression df=5 F=205.37087 P<1.37754E-4
	astrocytes	40	4		
	HEK	20	2		
	SK-N-BE	20	1		
	P75 KO neurons	20	2		
	wt neurons	30	2		
4b (D)	CHO	5538	1	trajs from 9 cells	
	astrocytes	69349	3	trajs from 23 cells	
	HEK	15144	1	trajs from 10 cells	
	SK-N-BE	3043	1	trajs from 7 cells	
	P75 KO neurons	11063	2	trajs from 7 cells	
	wt neurons	10619	1	trajs from 4 cells	
4c	naive	85	1	n are analyzed cells	One-way analysis of variance, Tukey's multiple comparison naive vs meva P<0.05
	mevastatin	100	1		

	cholesterol	86	1		naive vs chol P<0.001
4d	wt p75 + NGF	65387	4	trajs from 37 cells	Kruskal–Wallis test (P < 0.0001) followed by Dunn’s comparison of means (P < 0.001 considered as significant)
	wt p75 +meva +NGF	35441	2	trajs from 14 cells	
	wt p75 +chol +NGF	47116	2	trajs from 20 cells	
	mut p75 + NGF	103472	4	trajs from 38 cells	
	mut p75 +meva +NGF	39198	2	trajs from 15 cells	
	mut p75 +chol +NGF	40749	2	trajs from 20 cells	
4f	p75	21	3	n are cells	one-way ANOVA, Bonferroni comparison of means Df=3 F=3.600 P75 vs P75 +NGF P=P=0.0162
	P75 +NGF	25	3		
	mut P75	24	3		
	mut P75 +NGF	32	3		
5b	naive	153	1	n are cells	one-way ANOVA, Tukey’s comparison of means Df=2,426 F=188.4 P<10E-6 naive vs meva P<10E-4 naive vs chol P<10E-4
	meva	145	1		
	chol	131	1		
5c	naive	3	3	2064 neurons	one-way ANOVA, Tukey’s comparison of means Df=5,14 F=13.87 P<10E-6 Nt vs NT pro P=0.0013 NT vs meva P=0.4790 NV vs chol P=0.1953 meva vs meva pro P=0.9115 chol vs chol pro P=0.0007
	naive pro	3	3	1850 neurons	
	meva	3	3	686 neurons	
	meva pro	3	3	368 neurons	
	chol	5	5	552 neurons	
	chol pro	3	3	495 neurons	
5d	NT	3	3	4500 neurons	one-way ANOVA, Tukey’s comparison of means Df=5,16 F=60.77 P<10E-6 NT vs NT pro P=0.9814 P75 vs P75 pro P<10E-4 mut P75 vs mut P75 pro P=0.9998 P75 vs NT P=0.9907 mut P75 vs NT P=0.3386
	NT pro	3	3	5337 neurons	
	P75	4	4	4685 neurons	
	P75 pro	4	4	4601 neurons	
	mut P75	4	4	4248 neurons	
	mut P75 pro	4	4	3941 neurons	
5e	NT	4	4	1786 neurons	one-way ANOVA, Tukey’s comparison of means Df=5,18 F=0.01308 P>0.999 NT vs NT pro P>0.999 P75 vs P75 pro PP>0.999 mut P75 vs mut P75 pro PP>0.999 P75 vs NT P>0.999 mut P75 vs NT P>0.999
	NT pro	4	4	1848 neurons	
	P75	4	4	2676 neurons	
	P75 pro	4	4	2040 neurons	
	mut P75	4	4	1294 neurons	
	mut P75 pro	4	4	1030 neurons	
5f	NT	5	5	2843 neurons	one-way ANOVA, Tukey’s comparison of means Df=5,20 F=42.3 P<10E-6 NT vs NT pro P=0.8512 P75 vs P75 pro P<10E-4 mut P75 vs mut P75 pro P<10E-4 P75 vs NT P=0.9884 mut P75 vs NT P=0.9846
	NT pro	5	5	3984 neurons	
	P75	4	4	3731 neurons	
	P75 pro	4	4	3164 neurons	
	mut P75	4	4	3976 neurons	
	mut P75 pro	4	4	2801 neurons	
6c	wt	30	3	n are axons	one-way ANOVA, Kruskal–Wallis test, followed by Dunn’s comparison n=4,159 S=59.95 P<10E-5 KO vs wt P<10E-4 KO vs KO +P75 P<10E-4 KO vs KO +mut P75 P<10E-4 wt vs KO +P75 P>0.999 wt vs KO +mut P75 P>0.999
	KO	49	3		
	KO +P75	43	3		
	KO +mut P75	37	3		

6d	wt	30	3	n are branch points	one-way ANOVA, Kruskal-Wallis test, followed by Dunn's comparison n=4,159 S=59.05 P<10E-5 KO vs wt P<10E-4 KO vs KO +P75 P<10E-4 KO vs KO +mut P75 P<10E-4 wt vs KO +P75 P>0.999 wt vs KO +mut P75 P>0.999
	KO	49	3		
	KO +P75	43	3		
	KO +mut P75	37	3		
6e	wt	30	3	n are lateral growth cones	one-way ANOVA, Kruskal-Wallis test, followed by Dunn's comparison n=4,159 S=68.85 P<10E-5 KO vs wt P<10E-4 KO vs KO +P75 P<10E-4 KO vs KO +mut P75 P<10E-4 wt vs KO +P75 P>0.999 wt vs KO +mut P75 P>0.999
	KO	49	3		
	KO +P75	43	3		
	KO +mut P75	37	3		
6g	NT	37	2	n are growth cones	one-way ANOVA (Geisser-Greenhouse correction for unequal variance), Bonferroni comparison of means Df=5,312 F=18.13 P<10E-5 NT vs NT +proNGF P<0.999 P75 vs P75 +proNGF P<10E-4 mut P75 vs mut P75 +proNGF P<10E-4
	NT +proNGF	20	2		
	P75	62	2		
	P75 +proNGF	66	2		
	mut P75	83	2		
	mut P75 + proNGF	57	2		
7b	P75	19	2	n are neurons	one-way ANOVA, Kruskal-Wallis test, followed by Dunn's comparison N=4,105 S=39.86 P=9.16659E-5 P75 vs P75 +proNGF rank diff=-47.26 P<0.0001 mut P75 vs mut P75 +proNGF rank diff=-29.44 P=0.0003
	P75 +proNGF	15	2		
	mut P75	37	2		
	mut P75 +proNGF	34	2		
7e	P75 Dynasore	17	2	n are neurons	one-way ANOVA, Kruskal-Wallis test, followed by Dunn's comparison N=4,78 S=4.879 P=0.1808
	P75 Dynasore +proNGF	9	2		
	mut P75 Dynasore	38	2		
	mut P75 Dynasore +proNGF	14	2		
7f	EGFP	19	2	n are growth cones	one-way ANOVA, Bonferroni comparison of means Df=8,186 F=19.72178 P<10E-6 EGFP vs EGFP Dyn. P=1 EGFP vs EGFP pro P=1 P75 Dyn. vs EGFP Dyn. P=4.33635E-5 P75 Dyn. pro vs EGFP Dyn. P=9.02041E-5 mut P75 Dyn. vs EGFP Dyn. P=1.36495E-7 mut P75 Dyn. pro vs EGFP Dyn. P=2.89682E-7
	EGFP +proNGF	30	2		
	EGFP Dynasore	17	2		
	EGFP Dynasore +proNGF	26	2		
	P75 Dynasore	17	2		
	P75 Dynasore +proNGF	14	2		
	mut P75 Dynasore	41	2		
	mut P75 Dynasore +proNGF	31	2		
7h	Vehicle	12	2	n are neurons	Welch's test t=6.241 df=18.24 P<0.0001
	Pitstop	19	2		

7i	EGFP vehicle	23	2	n are growth cones	One-way ANOVA $F(3,135)=13.97$ $P<0.0001$ Tukey comparison of means EGFP vehicle vs P75 vehicle $P=0.9979$ EGFP Pitstop vs P75 Pitstop $P<0.0001$
	EGFP Pitstop	21	2		
	P75 vehicle	26	2		
	P75 Pitstop	69	2		
S1b	A1-P75	14	3	n are cells	Paired Student's t-test, two-tailed $t=-3.923$ $dF=13$ $P=0.0017$
	S6-P75	18	3		
S1d	$[10^{-3};10^{-2}]$ doxycycline	25	2	n are cells	Unpaired Student's t-test, two-tailed $t=8.647$ $dF=2$ $P=0.0131$
	$[>10^{-2};1]$ doxycycline	8	2		
S3	Qdot655	4994	1	trajs from 10 cells	NA
	Abberior635P	5086	3	trajs from 20 cells	
S5	wt p75NTR	180491	4	trajs from 43 cells	NA
	mut p75NTR	207280	4	trajs from 47 cells	
	dim p75NTR	108422	5	trajs from 43 cells	
S6a	photobleaching steps	267	3	spots from 15 cells	NA
	intensity histogram	273	3	spots from 15 cells	
S6b	wt p75NTR	536	3	n are spots from 15 cells	Multigaussian fit adj $r^2=0.97913$, reduced $\chi^2=42.86579$, ANOVA of regression $df=4,12$ $F=281.38763$ $P=2.20993E-11$
	mut p75NTR	764	3		Multigaussian fit adj $r^2=0.97319$, reduced $\chi^2=70.45649$, ANOVA of regression $df=5,14$ $F=218.69841$ $P=1.89826E-12$
	dim p75NTR	925	3		Multigaussian fit adj $r^2=0.98707$, reduced $\chi^2=592.07497$, ANOVA of regression $df=6,20$ $F=592.07497$ $P<10E-12$
S7	wt neurons	5544	1	trajs from 4 cells	Kruskal-Wallis test ($P < 0.0001$) followed by Dunn's comparison of means ($P < 0.001$ considered as significant)
	wt neurons + proNGF	7887	1	trajs from 5 cells	
	P75 KO neurons	11063	2	trajs from 7 cells	
	P75 KO neurons + proNGF	24593	2	trajs from 13 cells	
S8	statistics as in Fig. 4b				
S9	untransfected	2	2	2961 neurons	one-way ANOVA, Tukey's comparison of means $Df=5,6$ $F=119.7$ $P<0.0001$ untr vs untr pro $P=0.9122$ untr vs wt $P=0.0002$ untr vs mut $P=0.0509$ wt vs wt pro $P=0.0025$ del vs del pro $P=0.0086$
	untransfected_proBDNF	2	2	4876 neurons	
	wt P75	2	2	4291 neurons	
	wt P75_proBDNF	2	2	4941 neurons	
	mut P75	2	2	3356 neurons	
	mut P75_proBDNF	2	2	4064 neurons	
S10a	wt	49	2	n are axons	Mann-Whitney U test, $U=493$ $P<0.0001$
	P75 KO	49	2		
S10b	wt	6	2	n are fields	Mann-Whitney U test, $U=2$ $P=0.0027$
	P75 KO	8	2		
S10c	wt	10	2	n are fields	Mann-Whitney U test, $U=23$ $P=0.0433$
	P75 KO	10	2		
S11	EGFP	7	2	n are growth cones	one-way ANOVA, Tukey comparison of means $F(7,246)=12.35$ $P<0.0001$
	EGFP proNGF	18	2		
	EGFP Dynamin wt	14	2		

	EGFP Dynamin K44A	19	2		EGFP proNGF vs p75 proNGF P=0.0002 EGFP Dyn K44A vs P75 Dyn K44A P=0.0003 P75 vs P75 proNGF P<0.0001 P75 Dyn wt vs P75 Dyn K44A P<0.0001
	P75	45	2		
	P75 proNGF	32	2		
	P75 Dynamin wt	29	2		
	P75 Dynamin K44A	90	2		
S12	0.05 doxy	120	2	n are neurons	NA
	1 doxy	128	2		
	constitutive	117	2		
S13a	Wt 0	40	2	n are growth cones	one-way ANOVA, F(7,566)=10.23 P<0.0001 Tukey comparison of means wt 0 proNGF vs wt 0.05 proNGF P=0.041 wt 0.05 vs wt 0.05 proNGF P=0.4042 wt 1 vs wt 1 proNGF P<0.0001 wt con vs wt con proNGF P<0.0001
	Wt 0 proNGF	57	2		
	Wt 0.05	56	2		
	Wt 0.05 proNGF	60	2		
	Wt 1	110	2		
	Wt 1 proNGF	104	2		
	Wt const	61	2		
	Wt const proNGF	86	2		
	Mut 0	28	2		one-way ANOVA, F(7,913)=7.931 P<0.0001 Tukey comparison of means mut 0 proNGF vs mut 0.05 proNGF P=0.007 mut 0.05 vs mut 0.05 proNGF P=0.322 mut 1 vs mut 1 proNGF P<0.0001 mut con vs mut con proNGF P=0.0001
	Mut 0 proNGF	47	2		
	Mut 0.05	54	2		
	Mut 0.05 proNGF	47	2		
	Mut 1	68	2		
	Mut 1 proNGF	76	2		
Mut const	50	2			
Mut const proNGF	46	2			
S13b	S6-P75	37	2	n are growth cones	y=a*x+b a=26529±4710, b=98.57±579 r ² =0.4755 F(1,35)=31.73 P<0.0001

NA: not applicable